國立交通大學

電控工程研究所

碩 士 論 文

應用在太陽能光伏發電系統中的高效率全類比最大功率追蹤技術

Highly Efficient Analog Maximum Power Point Tracking (AMPPT) in a Photovoltaic System

研究生：楊智宇

指導教授：陳科宏 博士

中 華 民 國 一 百 年 九 月

應用在太陽能光伏發電系統中的高效率全類比最大功率追蹤技術

Highly Efficient Analog Maximum Power Point Tracking (AMPPT) in a Photovoltaic System

研 究 生：楊智宇　　Student：Chih-Yu Yang

指 導 教 授：陳科宏　　Advisor：Dr. Ke-Horng Chen

國 立 交 通 大 學

電 控 工 程 研 究 所

碩 士 論 文

A Thesis

Submitted to Institute of Electrical Control Engineering
College of Electrical and Computer Engineering
National Chiao Tung University
in partial Fulfillment of the Requirements
for the Degree of
Master
in

Electrical Control Engineering

September 2011

Hsinchu, Taiwan, Republic of China

中華民國一百年九月

應用在太陽能光伏發電系統中的高效率全類比最大功率追蹤技術

研究生：楊智宇　　指導教授：陳科宏 博士

國立交通大學 電控工程研究所 碩士班

摘　　要

本論文利用類比電路的設計，提出了一個可以應用於太陽能光伏(Photovoltaic)發電系統中的最大功率追蹤技術(Maximum Power Point Tracking, MPPT)。論文一開始先探討了太陽能板的非線性特性。太陽能板鑒於不同的外在溫度以及太陽光照度，因而存在著不同的最大功率點(Maximum Power Point, MPP)。這些受外在環境影響的非線性特性嚴重地影響了太陽能板發電效率。論文比較了現存的幾種最大功率追蹤技術之間的優劣，並提出了一個同時具有高追蹤速度以及高追蹤效率的最大功率追蹤技術。太陽能發電系統的電壓電流操作範圍受到外在環境因素的影響相當明顯，其操作範圍也因此相當大。因此在這篇論文中，作者提出了一個具有大計算範圍的電流乘法器來滿足在最大功率追蹤上斜率計算電路的需求。除此之外，太陽能板的最大功率點以及發電效能常受到周遭建築物或是雲的遮蔽而改變。全域最大功率追蹤技術(Global Maximum Power Point Tracking, GMPPT)可以進一步的實現在這篇論文所提出的最大功率追蹤技術上，來提升整個太陽能發電系統的健全性與實用性。在論文的最後，相關的模擬以及實驗結果證明了所提出的最大功率追蹤技術可達到追蹤效率 97.3%。除此之外，所提出的太陽能發電系統並可將太陽能所產生的電力反饋回市電上，進而拓展整個太陽能光伏發電系統的應用層面。

Highly Efficient Analog Maximum Power Point Tracking (AMPPT) in a Photovoltaic System

Student：Chih-Yu Yang　　Advisor：Dr. Ke-Horng Chen

Institute of Electrical Control Engineering
National Chiao-Tung University

ABSTRACT

A compact-size analog maximum power point tracking (AMPPT) technique is proposed in this thesis for high power efficiency in the photovoltaic (PV) system. Several MPPT techniques are studied at first to compare their pros and cons. The characteristics of solar array are introduced as well to address the difficulties when utilizing the solar energy. Combining the existing MPPT approaches, the thesis presents a fast and accurate tracking performance. The shading effect, which undermines the efficiency of solar array, is also discussed. The proposed MPPT technique can be further improved by global maximum power tracking (GMPPT) algorithm to guarantee its robustness. Here, a wide-range current multiplier, which tracks the maximum power point (MPP) in the solar power system, is implemented to detect the power slope condition of solar array. Simulation and experiment results show that the proposed MPPT technique can rapidly track the MPP with a high tracking efficiency of 97.3%. Furthermore, the proposed system can connect to the grid-connected inverter to supply AC power.

誌　謝

在交大碩士班的生涯，轉眼間就快結束了。首先要感謝的是一路上提拔以及支持我的指導教授 陳科宏老師。在研究方面，老師從碩一的一開始就給我了這個頗具挑戰性的研究方向，因為是一個全新的研究主題，可以參考的文獻以及可以請教的學長姐有限，老師總是我遇到問題時第一個會去請教的對象。一邊在老師辦公室喝著老師親手煮的咖啡，一邊面對投影片上總總的問題，老師總是會指引我一個方向，讓我自己去找答案，進而從解決問題的過程中，發掘到更多的新知識。除此之外，也因為得到老師百分之百的支持，有機會利用碩二結束後的一年時間，交換到德國慕尼黑工業大學一年，見識到了國外大學的上課風氣以及體驗到了國外生活的種種經驗。

除此之外，還要感謝的是實驗室裡的學長姊、學弟妹們。昱輝學長除了總是可以在我研究上遇到難題時，關鍵的給予建議，也時常一起在深夜的工五八樓窗台旁，一起聊著過去大學時的懷舊時光，一起訴說著生活上面對到的難題，也一起計劃著出國旅行的種種驚奇!俊禹、緯權、柄境、士榮、裕農、福貴學長們在研究上的指導，玉萍、以萍、冠宇、淳仁、暐中等學弟妹們在生活樂趣上的分享。

另外還要感謝我最摯愛的爸媽以及熊小姐，爸媽總是無私的支持我的任何決定，無論是在經濟上或是生活上，熊小姐則是一直能體諒我在研究上的辛苦，適時的給我加油鼓勵，你們是我在台灣及國外生活時最大的精神支柱!

最後還要感謝的是大學以及研究所這幾年時間，無論是在國外或是台灣認識的朋友、同學們，你們讓我的求學生涯豐富精采也值得回味!

楊智宇

國立交通大學 新竹 台灣

中華民國一百年九月

Content

Figure Caption

Table Caption

Chapter 1

Introduction

1.1 The Solar Energy and its Applications

The global warming crisis has recently drawn worldwide public attention to issues related to energy conservation and alternative energy. Several energy conservation methods, such as energy recycling [1] and energy harvesting techniques [2], have been proposed to reduce unnecessary energy waste from commercial appliances. In addition, alternative energy, such as thermal [3], wind [4], or solar energy [5], is renewable and addresses pollution problems. Solar energy presents the advantages of low maintenance cost and pollution-free characteristics. These are keys to solving worsening global warming and reducing greenhouse gas emissions. Thus, this alternative energy has been gaining increasing popularity in numerous countries.

Solar energy may not be the most efficient choice with regard to energy production. Nevertheless, it still outweighs other kinds of energy, such as nuclear, coal, and gas energy, because it causes zero pollution, has no moving parts, and allows for easy maintenance. Despite these advantages, the overall energy production cost for solar energy is still too high compared with that incurred from gas or oil production. High costs restrict the wide-ranging global application of solar power systems. Generally, the low power efficiency of a solar power system is generally attributed to two factors. One is the conversion efficiency of the solar cell. The other is

related to the power efficiency of the system, or more specifically, the power efficiency on the power stage. The improvement of solar cell materials and relevant technology has continuously elevated the conversion efficiency of solar cells [6]. Conversion energy is reported to reach around 30% in today's commercial products when a specific material is adopted [7]. Furthermore, enhancing the power efficiency of solar power systems enables the improvement of the efficiency of the power stage and the extraction of substantial energy from solar panels. The nonlinear physical characteristics of solar arrays, however, are inevitable obstacles to the highly efficient energy utilization of solar power systems.

The maximum available power supplied by a solar array depends on solar irradiation level and ambient temperature [8]. In practice, both these factors are difficult to precisely predict and measure. Thus, contemporary photovoltaic (PV) products, such as PV inverters [9] or solar chargers [10], are usually integrated with maximum power point tracking (MPPT) technique to extract the highest energy volume from solar arrays. Several MPPT algorithms exist [11]-[12]. Some of them are implemented using a microcontroller [13], field programmable gate array [14], and digital signal processors [15]. Others are implemented using analog or mixed signal methods [16]-[17]. For instance, in [18], a small-signal sinusoidal perturbation is injected into the switching frequency to compare the AC component. The average value of the solar array voltage is used to locate the maximum power point (MPP). In [19], the authors track the MPP by introducing a small-signal sinusoidal perturbation into the duty cycle of the switch and comparing the maximum variation in the input voltage and the

voltage stress on the switch. Ref. [20] uses the extremum-seeking control method to track the MPP. All of these tracking methods can exhibit high tracking efficiency. Unfortunately, they are implemented by discrete components instead of an integrated circuit (IC). In [21], a dual-module–based tracking technique, which compares the voltage and current difference between two solar arrays to track the MPP, is proposed. This method, however, increases hardware costs because each solar array has to be controlled by an individual tracker.

References [22] and [23] use the pilot cell to assist tracking. Nevertheless, the pilot cell should match the characteristics of the main solar array. In [24], a tracking solution is used to address the problems encountered during rapidly changing weather conditions. The technique incorporates an additional measurement of power in the middle of the MPPT sampling period. Furthermore, one can also use the information of the solar array, such as the diode quality factor and the reverse saturation current, to track the MPP [25]. Some methods combine two different tracking techniques to gain advantages. In [26] and [27], two tracking techniques are combined to improve tracking efficiency. The system switches between two tracking methods according to irradiation levels.

1.2 Motivation

Numbers of maximum power point tracking techniques exist in today's commercial products and present in lots of literatures as mentioned before. However, most of the existing techniques are implemented by either the discrete components or the microcontrollers. In this proposed paper, a MPP tracker using single chip controller IC is proposed. The proposed MPP tracker features fast tracking speed and high tracking accuracy. In addition, the proposed system includes a boost DC-DC converter and a grid-connected PV inverter as well to convert the solar energy into the power grid for further use [28].

1.3 Thesis Organization

The thesis is organized as follows. In Chapter 2, the characteristics of the solar array are discussed in detail to show nonlinear behaviors and relevant cause factors. Some existing tracking algorithms are also discussed. Chapter 3 introduces the proposed MPPT algorithm used to extract the highest volume of energy from solar arrays. Circuit implementation is presented in Chapter 4 to demonstrate the proposed wide-range current multiplier used in the PV system intended for improving tracking efficiency. The simulation and measurement results, shown in Chapter 5, confirm the functionality and efficiency of the proposed MPPT system. Finally, Chapter 6 concludes the studies.

Chapter 2

Maximum Power Point Tracking and the Proposed Solar System

2.1 The Characteristics of PV Module

PV cell or PV module is typically made of semiconductor materials, which is used to convert solar energy into electricity for further use. Based on different materials and different manufacture processes, there exists several PV cell types nowadays in the market and the conversion efficiency varies from each other. TABLE 2.1 summarizes the conversion efficiencies of different PV cell types. The conversion efficiency, however, is limited up to 30%. Considering the manufacture cost and the conversion efficiency, single crystalline silicon cell and multi-crystalline silicon cell are the two mostly used PV cells in today's market.

TABLE 2.1 Efficiency Comparisons of Different PV Cells

Cell Material	**Cell Efficiency (%)**	**Module Efficiency (%)**
Single-Crystalline Silicon	22	10-15
Multi-Crystalline Silicon	18	9-12
Thin-Film Amorphous Silicon	13	10
Thin-Film Copper IndiumDiselenide	19	12
Thin-Film Cadmium Telluride	16	9
High-Efficiency and ConcentratorConcepts(III-V)	30	17

The characteristics of PV module vary with respect to different irradiation levels and different ambient temperatures. A simplified equivalent circuit [29] in Fig. 2.1 can facilitate the investigation of the nonlinear behaviors of PV module. The equivalent circuit consists of a current source, I_L, which suggests the light-generated current; a diode, D_1, which emulates the PN junction of a real PV cell; a series resistor, R_s, and a parallel resistor, R_p, which symbolize the parasitic series resistance and the parasitic parallel resistance on the PV module, respectively. The voltage generated at the terminals, V_{PV}, is the voltage of the PV module, which can be multiplied through series-connected PV modules. Moreover, the current flowing out from the terminals, I_{PV}, is the current of the PV module. The relationship between V_{PV} and I_{PV} can be shown in the following equations [30].

$$I_{PV} = I_L - I_{os}\left\{\exp\left[\frac{q}{AkT}\left(V_{PV} + I_{PV}R_s\right)\right] - 1\right\} - \frac{V_{PV} + I_{PV}R_s}{R_P} \tag{2.1}$$

$$I_{os} = I_{or}\exp\left[\frac{qE_{GO}}{Bk}\left(\frac{1}{T_r} - \frac{1}{T}\right)\right]\left[\frac{T}{T_r}\right]^3 \tag{2.2}$$

$$I_L = \frac{S\left[I_{SC} + K_I\left(T - 25\right)\right]}{100} \tag{2.3}$$

where

I_{PV}: PV module output current;

V_{PV}: PV module output voltage;

R_p: parallel resistor;

R_s: series resistor;

I_{os}: PV module reversal saturation current;

A, B: ideality factors;

T: temperature (℃);

k: Boltzmann's constant;

I_L: light-generated current;

q: electronic charge;

K_I: short-circuit current temperature coefficient at I_{SC};

S: solar irradiation (W/m^2);

I_{SC}: short-circuit current at 25℃ and 1000 W/m^2;

E_{GO}: bandgap energy for silicon;

T_r: reference temperature;

I_{or}: saturation current at the temperature of T_r;

The equations verify that the characteristics of PV module depend on both temperature and solar irradiation. Fig. 2.2 and Fig. 2.3 show the IV curves sketched under different circumstances, which are different irradiation levels and different ambient temperatures. Under different irradiation levels, as shown in Fig. 2.2, the maximum power point (P_{MPP}) increases as the solar irradiation increases, which means P_{MPP} is proportional to the solar irradiation level. For different ambient temperatures, the IV curves act like Fig. 2.3. As can be seen in this figure, P_{MPP} decreases when the ambient temperature increases. That is to say, P_{MPP} is inverse proportional to the ambient temperature. These nonlinear characteristics of PV module are crucial for analyzing and designing the PV system, especially for the maximum power point tracker.

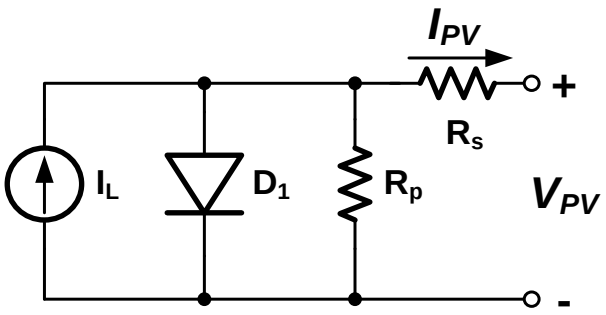

Fig. 2.1. Equivalent circuit of PV module.

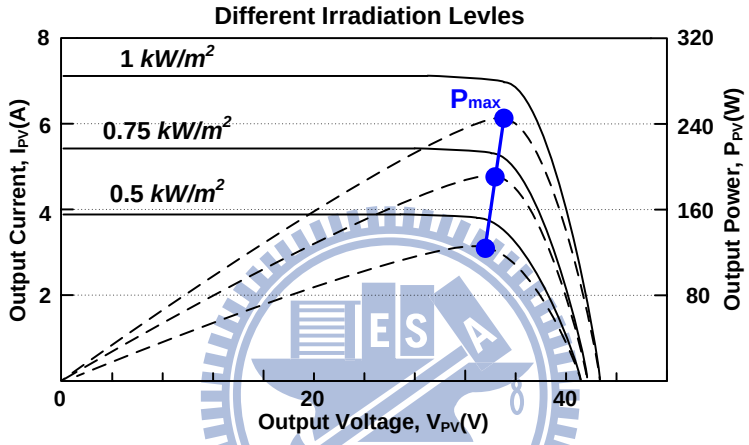

Fig. 2.2. Characteristic curve of solar panel with respect to different irradiation levels.

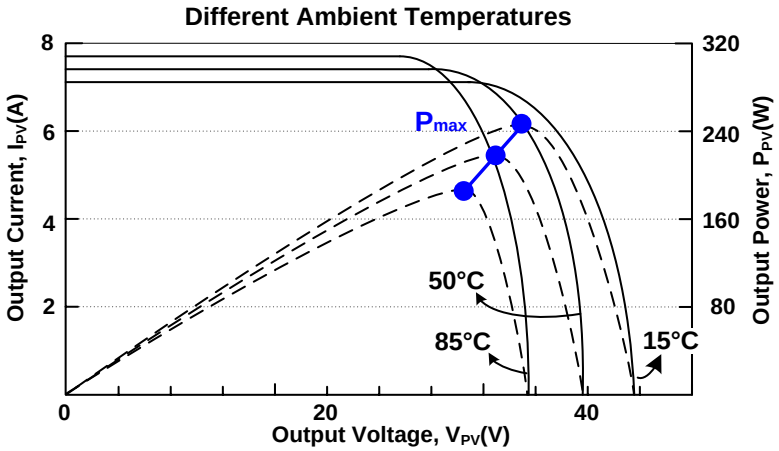

Fig. 2.3. Characteristic curve of solar panel with respect to different ambient temperatures.

2.2 MPPT Topology Studies

There exist numerous maximum power point tracking algorithms in today's market. This section discusses some of them and addresses their pros and cons.

2.2.1 Perturbation and Observation (P&O) / Hill Climbing

Perturbation and observation (P&O) method and hill climbing method are the two most common maximum power point tracking algorithms. P&O involves a perturbation in the operating voltage, and hill climbing, on the other hand, perturbs the duty ratio of the power converter connected to the PV modules. In the case of a PV module connected to a power converter, perturbing the duty ratio of power converter perturbs the PV module current and as a consequence perturbs the PV module voltage. Therefore, perturbation and observation method and hill climbing method are two tracking methods envisioning the same fundamental idea.

It can be seen in Fig. 2.2 and Fig. 2.3 that incrementing the voltage increases the power when the operating point is on the left side of the maximum power point (MPP) and decreases the power when the operating point is on the right side of the MPP. Therefore, if there is an increase in power, the subsequent perturbation should be remained the same to reach the MPP. Conversely, if there is a decrease in the power, the perturbation should be reversed to reach the MPP. TABLE 2.2 summarizes the ideas of perturbation and observation method and hill climbing method.

TABLE 2.2 Summary of P&O and Hill Climbing Algorithm

Perturbation Direction	Change in Power	Next Perturbation Direction
Positive	Positive	Positive
Positive	Negative	Negative
Negative	Positive	Negative
Negative	Negative	Positive

The process is repeated periodically until the MPP is reached. The system then oscillates around the MPP. The oscillation can be minimized by reducing the perturbation step size. However, a smaller perturbation step size slows down the tracing speed. There exist still other limitations that degrade the MPPT efficiency. For instance, as the amount of sunlight decreases, the Power-Voltage curve flattens out, as seen in Fig. 2.2. This makes it difficult for the MPPT to discern the location of the MPP, owing to the small change in power with respect to the perturbation of the voltage.

2.2.2 Incremental Conductance

The incremental conductance method is based on the fact that the slope of the PV module power curve is zero at the MPP, positive on the left of the MPP, and negative on the right, as summarized in TABLE 2.3.

TABLE 2.3 Slope Condition of the Operating Point

Position of the Operating Point	Slope of the Power Curve
@ MPP	$\frac{dP}{dV}=0$
Left Side of MPP	$\frac{dP}{dV}>0$
Right Side of MPP	$\frac{dP}{dV}<0$

Since

$$\frac{dP}{dV} = \frac{d(IV)}{dV} = I + V\frac{dI}{dV} \cong I + V\frac{\Delta I}{\Delta V} \tag{2.4}$$

TABLE 2.3 can be reformulated into the following TABLE 2.4. The MPP can, as a result, be tracked by comparing the instantaneous conductance ($\frac{I}{V}$) to the incremental conductance ($\frac{\Delta I}{\Delta V}$).

TABLE 2.4 Equations of Determining the MPP

Position of the Operating Point	**Equation of Determining the MPP**
@ MPP	$\frac{\Delta I}{\Delta V} = -\frac{I}{V}$
Left Side of MPP	$\frac{\Delta I}{\Delta V} > -\frac{I}{V}$
Right Side of MPP	$\frac{\Delta I}{\Delta V} < -\frac{I}{V}$

Fig. 2.4 shows the flow chart of the incremental conductance tracking technique. V_{op} is the reference operating voltage at which the PV module is forced to operate. At the MPP, V_{op} is equal to V_{MPP}, the maximum power point voltage. As long as the MPP is reached, the operation of the PV module is maintained at this point unless a change in ΔI is detected, which might indicate a change of the ambient temperature or a change of the sunlight irradiation level. If this scenario occurs, the tracking algorithm, judging the inequity equations, either increases or decreases V_{op} to track the new MPP. The increment size determines the tracking speed. Fast tracking can be achieved with larger incremental steps but the system might not operate exactly at the MPP, instead oscillates around it. As a result, there is a tradeoff between the tracking speed and the tracking accuracy.

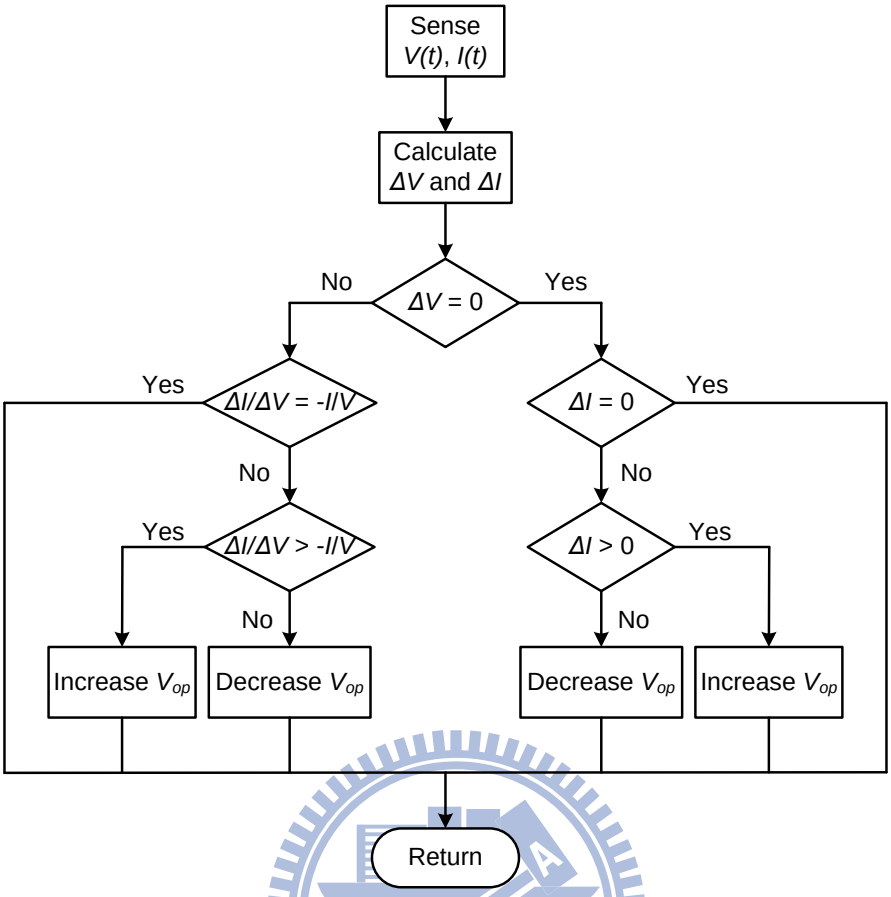

Fig. 2.4. The flow chart of incremental conductance algorithm.

2.2.3 Fractional Open-Circuit Voltage

The near linear relationship between the maximum power point voltage, V_{MPP}, and the open-circuit voltage, V_{OC}, of the solar array, under varying irradiation and temperature levels, has given rise to the fractional V_{OC} method.

$$V_{MPP} \approx k_V V_{OC} \tag{2.5}$$

where k_V is a constant of proportionality. Since k_V is dependent on the characteristics of the solar array being used, it usually has to be computed beforehand by empirically determining V_{MPP} and V_{OC} for the specific solar array at different irradiance and temperature levels. The factor k_V has been reported to be around 0.7.

Once the factor k_V is determined, V_{MPP} can be computed by Eq. (2.5) with V_{OC} measured periodically by momentarily shutting down the power converter. Since Eq. (2.5) is only an approximation, the solar array technically never operates at the true MPP. Depending on the application of the PV system, this can sometimes be accurate enough for the system. Even if fractional V_{OC} is not a true MPPT technique, it is very easy and cheap to implement as it does not necessarily require DSP or microcontroller control.

2.2.4 Fractional Short-Circuit Current

Fractional short-circuit current, I_{SC}, results from the fact that, under varying atmospheric conditions, the maximum power point current, I_{MPP}, is approximately linearly related to the I_{SC} of the solar array.

$$I_{MPP} \approx k_I I_{SC} \tag{2.6}$$

where k_I is a proportionality constant. Just like in the fractional V_{OC} technique, k_I has to be determined according to the solar array in use. The constant k_I is generally between 0.78 and 0.92.

Using the fractional short-circuit current method to track the maximum power point seems to be easy to implement. However, measuring I_{SC} during operation is problematic. One problem encountered is that an additional switch usually has to be added to the power converter to periodically short the solar array so that I_{SC} can be measured using a current sensor. This increases the number of components and the hardware cost. Another problem is that the power output is not only reduced when detecting I_{SC} but also because the MPP is never precisely matched as indicated by Eq. (2.6).

2.2.5 DC-Link Capacitor Droop Control

DC-link capacitor droop control is an MPPT technique that is specifically designed to work with a PV system that is connected in parallel with an AC system line as shown in Fig. 2.5.

The duty ratio of an ideal converter is given by

$$Duty = 1 - \frac{V_{PV}}{V_{link}} \tag{2.7}$$

where V_{PV} is the voltage across the PV array and V_{link} is the voltage across the DC link. If V_{link} is kept constant, increasing the current going into the inverter increases the power coming out of the boost converter and in consequence increases the power coming out of the solar array. While the current is increasing, the voltage V_{link} can be kept constant as long as the power required by the inverter does not exceed the maximum power available from the solar array. If that is not the case, V_{link} starts drooping. Right before that point, the current control command I_{peak} of the inverter is at its maximum and the solar array operates at the MPP. The AC system line current is fed back to prevent V_{link} from drooping and *Duty* is optimized to bring I_{peak} to its maximum, thus achieving MPPT.

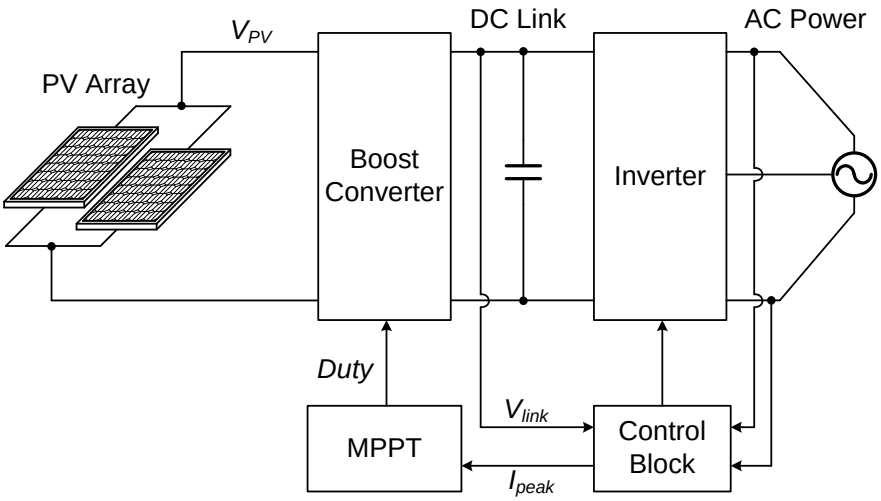

Fig. 2.5. Schematic of DC-link capacitor droop control MPPT.

2.2.6 Load Current/Load Voltage Maximization

The purpose of MPPT technique is to maximize the power coming out of the solar array. When the solar array is connected to a power converter, maximizing the solar array power maximizes the output power at the load of the converter as well. Conversely, maximizing the output power of the converter should maximize the solar array power, assuming a lossless converter is used.

Most loads can be of voltage-source type, current-source type, or resistive type. Therefore, for almost all loads of interest, it is adequate to maximize either the load current or the load voltage to maximize the load power. Nevertheless, operation exactly at the MPP is almost never achieved for the reason that this MPPT method is based on the assumption that the power converter is lossless.

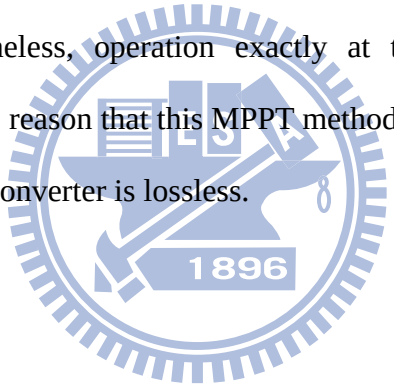

2.2.7 Pilot Cell

In the pilot cell MPPT algorithm, the fractional voltage or current method is used, the point is that the open-circuit voltage or short-circuit current measurements are made on a small solar cell, called a pilot cell, which has the same characteristics as the cells in the larger solar arrays. The measurement results of the pilot cell can be used by the MPPT to operate the main solar array at its MPP, eliminating the loss of power during the V_{OC} or I_{SC} measurement. However, the fractional factor either K_V or K_I is inconstant under varying environmental circumstances. As a result, the tracking precision is greatly reduced. Furthermore, this method has a logistical drawback in that the solar cell parameters of the pilot cell

must carefully match to those of the main solar array. Thus, each pilot cell and solar array pair must be precisely calibrated, which increase the cost of the system.

2.2.8 Model-Based Tracking

If the values of the parameters in Eq. (2.1)~(2.3) are known for a given solar cell, the solar cell's current and voltage could be calculated from measurements of the sunlight irradiation and temperature of the solar cell. The maximum power voltage could then be calculated directly, and the solar array operating voltage could be simply set equal to V_{MPP}. Such algorithm is commonly called a model-based MPPT algorithm. Although appealing, model-based MPPT is usually not practical because the values of the cell parameters are not known with certainty, and in fact can vary significantly between cells from the same production run.

2.2.9 Fuzzy Logic Control

Microcontrollers have made using fuzzy logic control popular for MPPT over the last decade. Fuzzy logic controllers have the advantages of working with imprecise inputs, not needing an accurate mathematical model, and handling nonlinearity.

Fuzzy logic control generally consists of three stages: fuzzification, rule base table lookup, and defuzzification. During fuzzification, numerical input variables are converted into linguistic variables based on a membership function. The membership function is sometimes made less symmetric to give more importance to specific fuzzy levels.

The inputs to a MPPT fuzzy logic controller are usually an error E and a change in error ΔE. The user has the flexibility of choosing how to compute E and ΔE . Since dP/dV vanishes at the MPP, uses the approximation

$$E(n)=\frac{P(n)-P(n-1)}{V(n)-V(n-1)} \tag{2.8}$$

and

$$\Delta E = E(n)-E(n-1) \tag{2.9}$$

Once E and ΔE are calculated and converted to the linguistic variables, the fuzzy logic controller output, which is typically a change in duty ratio ΔD of the power converter, can be looked up in a rule base table. The linguistic variables assigned to ΔD for the different combinations of E and ΔE are based on the power converter being used and also on the knowledge of the user.

In the defuzzification stage, the fuzzy logic controller output is converted from a linguistic variable to a numerical variable again using a membership function. This provides an analog signal that will control the power converter to the MPP.

MPPT fuzzy logic controllers have been shown to perform well under varying atmospheric conditions. However, their effectiveness depends a lot on the knowledge of the user or control engineer in choosing the right error computation and coming up with the rule base table.

2.2.10 Neural Network

Another MPPT algorithm well adapted for microcontrollers is by the method of neural network. Neural network commonly have three

layers: input, hidden, and output layers as shown in Fig. 2.6. The number of nodes in each layer varies and is user-dependent. The input variables can be solar array parameters such as V_{OC} and I_{SC}, atmospheric data like irradiation and temperature, or any combination of these. The output is usually one or several reference signals like a duty cycle signal used to drive the power converter to operate at the MPP.

How close the operating point gets to the MPP depends on the algorithms used by the hidden layer and how well the neural network has been trained. The links between the nodes are all weighted. The link between nodes *i* and *j* is labeled as having a weight of w_{ij} in Fig. 2.6. To accurately identify the MPP, the w_{ij}'s have to be carefully determined through a training process, whereby the solar array is tested over months or years and the patterns between the inputs and outputs of the neural network are recorded.

Since most solar arrays have different characteristics, a neural network has to be specifically trained for the solar array with which it will be used. The characteristics of a solar array also change with time, implying that the neural network has to be periodically retrained to guarantee an accurate MPPT.

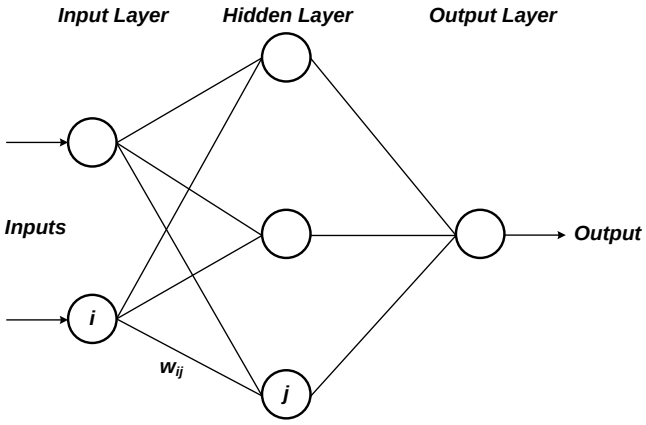

Fig. 2.6. Structure of the neural network.

TABLE 2.5 summarizes a comparison between the mentioned maximum power point tracking algorithms based on the characteristics of solar array dependence, the genuineness of the MPP, the tracking speed and also the design and implementation complexity.

TABLE 2.5 Comparisons between Different MPPT Techniques

MPPT Technique	**PV Array Dependence**	**True MPP**	**Tracking Speed**	**Design Complexity**
Perturbation and Observation / Hill-Climbing	Independent	Yes	Varies	High
Incremental Conductance	Independent	Yes	Varies	High
Fractional Open-Circuit Voltage	Dependent	No	Fast	Low
Fractional Short-Circuit Current	Dependent	No	Fast	Low
DC-Link Capacitor Droop Control	Independent	No	Medium	Low
Load Current / Load Voltage Maximization	Independent	No	Fast	Low
Pilot Cell	Independent	No	Varies	High
Model-Based Tracking	Dependent	Yes	Fast	High
Fuzzy Logic Control	Dependent	Yes	Fast	High
Neural Network	Dependent	Yes	Fast	High

2.3 The Proposed MPPT Solar System

In this thesis, an analog MPPT circuit with low-cost feature and high tracking efficiency is proposed. The proposed PV system is illustrated in Fig. 2.7. The proposed system includes a boost DC-DC converter, which serves the purpose of not only tracking the maximum power point of the solar arrays but also regulating the DC-link voltage, V_{BUS}. The boost converter controller consists of a scaling circuit, an Open-Circuit Tracking (OCT) enable circuit, a sample/hold circuit, a slope detection circuit, a 7-bit up-down counter, and a PWM generator. Furthermore, the proposed PV system includes a grid-connected PV inverter as well to convert the solar energy to the power grid for further use. The full bridge inverter is controlled by a microcontroller. The islanding effect detection, in addition, is executed by the inverter controller as well to ensure the safety of the maintenance personnel.

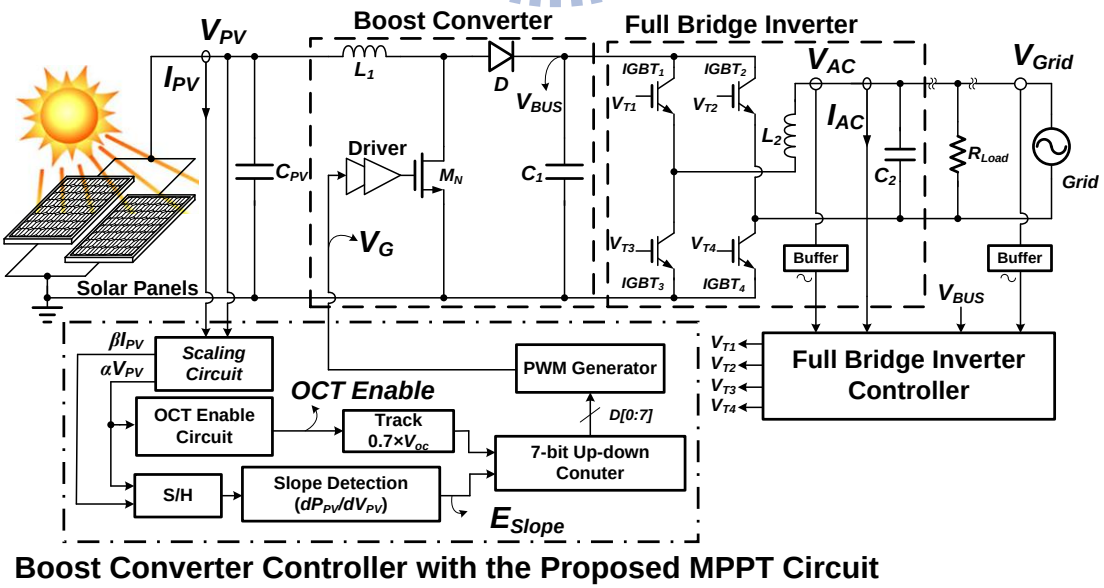

Fig. 2.7. The proposed grid-connected PV system.

Chapter 3

The Proposed MPPT Algorithm

3.1 The Pros and Cons of Voltage-Based Tracking Algorithm

As shown in Fig. 3.1 and Fig. 3.2, both the photovoltaic voltage and the photovoltaic current at the MPP can represent the MPP. For a particular operating condition, the control of MPPT normally regulates either the voltage or the current to a certain value that represents the local MPP. However, the mapping between MPP and these variables is time variant, as it is a function of changing irradiation and temperature. Ideally, however, this relationship is constant or changes slowly within a range. The photovoltaic voltage is a preferable control variable when it comes to the maximum power point tracking. The advantages of the voltage-based tracking are described in the following paragraph.

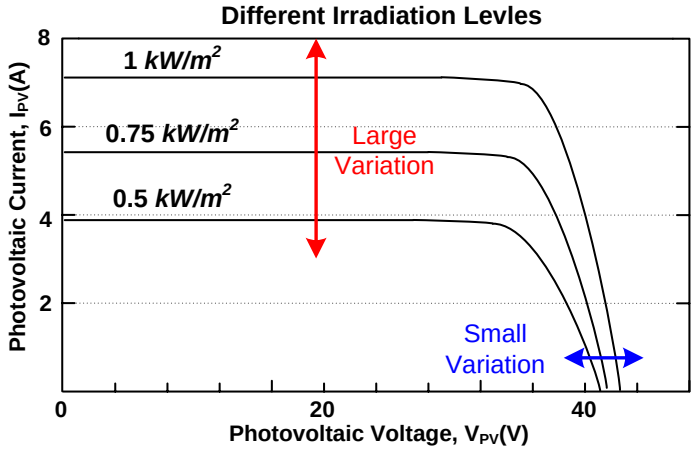

Fig. 3.1. Photovoltaic current vs. photovoltaic voltage under different irradiation levels.

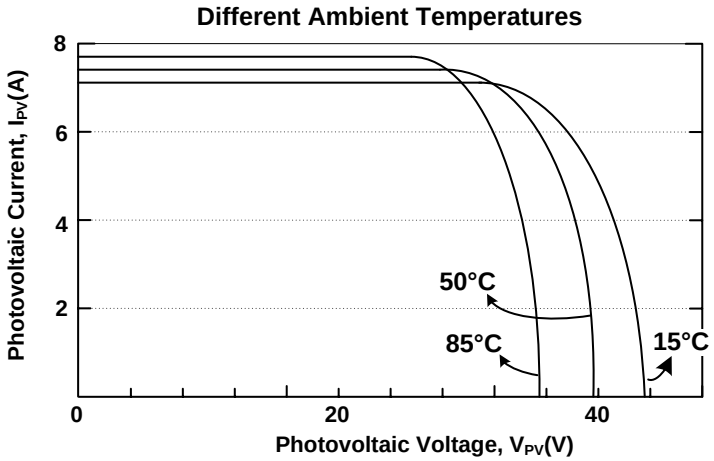

Fig. 3.2. Photovoltaic current vs. photovoltaic voltage under different ambient temperatures.

Changing radiation causes the photovoltaic current to vary dramatically, as illustrated in Fig. 3.1. The fast dynamic of insolation is usually caused by the cover of mixed rapidly moving clouds. If the photovoltaic current is used as the set point, the MPPT requires a fast dynamic to follow a wide operating range from 0A to the short-circuit current because the current is heavily dependent on weather conditions. In contrast, the changing insolation only slightly affects the voltage of MPP. Fig. 3.2 shows that the cell temperature is the dominant factor varying the voltage of MPP when the temperature changes. However, cell temperature has a slow dynamic and is always within a certain range.

Unlike the current of MPP, the photovoltaic voltage of MPP is usually bounded to 70%~82% of the open-circuit voltage. This gives the tracking range a lower bound and an upper limit. When regulation of the photovoltaic voltage is implemented, the MPPT can quickly decide the initial point according to the percentage of the open-circuit voltage.

The photovoltaic current value at MPP is close to around 86% of the short-circuit current. Because the photovoltaic current dramatically varies

with insolation, the transient response of MPPT can occasionally cause the photovoltaic current to reach its saturation point, which is the short-circuit current. This shall be prevented because its nonlinearity causes a sudden voltage drop and results in power losses. However, for the regulation of photovoltaic voltage, the voltage saturations can be easily avoided because a controller knows the operating range is bounded around 70%~82% of the open-circuit voltage. Furthermore, a good-quality measurement of voltage signal is cheaper and easier than that of current measurement. Considering all the benefits of the voltage-based tracking aforementioned, as a result, the voltage-based tracking algorithm is preferred than the current-based tracking.

The voltage-based tracking technique, aside from the advantages of robustness and low solar irradiation dependence, holds also the advantage of fast tracking speed and low implementation complexity.

According to the relationship between the maximum power point voltage (V_{MPP}) and the open-circuit voltage (V_{OC}), the maximum power point tracker can take the advantage of this attribute to tack the MPP with high tracking speed. As illustrated in Fig. 3.3, the operating point can quickly jump to the point $V_{MPP(approx)}$ near the MPP if the open-circuit voltage is known. The tracker easily calculates the voltage of MPP from the information of open-circuit voltage. This can be achieved simply by dividing or multiplying the open-circuit voltage.

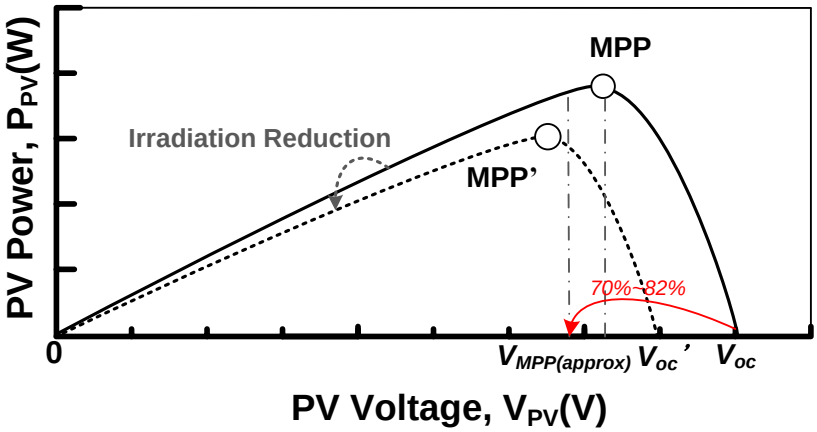

Fig. 3.3. The concept of voltage-based MPPT technique.

When the weather condition changes, say the irradiation reduces, the tracker has to disconnect the solar array and the power converter to create an open circuit on the system. This way, the new open-circuit voltage (V_{OC}'), as indicated in Fig. 3.3, is detected. After getting the information of the new open-circuit voltage, the tracker can further calculate the new maximum power point (*MPP'*) and therefore regulate the operating point to be around this point. All in all, the voltage-based tracking algorithm benefits from its low design complexity, only a divider or a multiplier is needed to calculate the maximum power point. The fast tracking speed is also guaranteed in this technique, since there is no complicated calculation and iteration.

The voltage-based tracking algorithm, on the other hand, has some undesirable drawbacks as well. For example, the low power efficiency and the poor tracking accuracy.

The working principle of the voltage-based tracking technique is based on both the open-circuit voltage and the pre-determined percentage between maximum power point voltage and the open-circuit voltage. In order to constantly track the maximum power point, the open-circuit voltage of the

solar array needs to be updated periodically. Therefore, one has to disconnect the connection between the solar array and the power converter so that the real time open-circuit voltage can be recorded. In this way, the power delivery path between the solar array and the output stage is interrupted. It causes power loses as a result. Namely, the power delivery is discontinuous on the PV system and low power efficiency is presented, which is obviously undesirable for a PV system.

The second obstacle of the voltage-based tracking technique toward its perfection is the low tracking accuracy. As mentioned before in Chapter 2, the voltage-based tracking technique depends on the information of open-circuit voltage and the pre-determined or pre-measured coefficient k_V. This coefficient, however, depends greatly on the manufacture material, the sunlight intensity, the environmental temperature and other factors. These factors are either time-varying or temperature-varying. As a result, it makes the determination and the measurement of the coefficient extremely difficult. Even though one can determine a desirable coefficient for a system, the environmental parameters, temperature, insolation, etc., vary along with the time, this makes the pre-determined coefficient inaccurate. Therefore, a high tracking accuracy cannot be guaranteed when the voltage-based tracking technique is used.

3.2 The Pros and Cons of Perturbation and Observation Tracking Algorithm

The perturbation and observation tracking technique takes the advantage of calculating the slope of the power-voltage characteristic curve

to determine the maximum power point. Once the slope condition is determined, the perturbation direction can be consequently decided. It forces the system to operate toward the maximum power point. Based on this tracking idea, the tracking accuracy or the tracking effectiveness is guaranteed even under a varying environmental condition. The varying environmental condition changes the power-voltage characteristic curve and undoubtedly alters the maximum power point. To find out the new maximum power point, the perturbation and observation technique recalculates the slope of the new characteristic curve and determines the next perturbation direction. In this way, the changing atmospheric factors do not affect the tracking functionality. Instead, a high tracking accuracy can be further ensured with smaller perturbation steps.

The downsides of the perturbation and observation tracking technique, however, are the oscillation problem, low tracking speed, and the demanding design complexity.

Since the working principle of the perturbation and observation algorithm is to change the operating point step by step, the system can never operate exactly at the maximum power point. Instead, the operating point jumps back and forth around the actual maximum power point. This, therefore, causes an oscillation problem when the system reaches near the maximum power point. The power delivery loss and fluctuation, as a result, present on the PV system.

Before concluding the next perturbation direction, the controller has to deliberately calculate the slope of the characteristic curve at that time instant. This slows down the entire tracking process, compared to the voltage-based tracking algorithm. However, a faster tracking speed using

perturbation and observation method can still be achieved if the variable perturbation step method is used. As shown in Fig. 3.4, the size of perturbation step is not fixed. Variable step size is used to accelerate the tracking process. The farer the operating point away from the maximum power point, the larger the perturbation step size is. When the operating point is near the maximum power point, a smaller step size is used to guarantee an accurate tracking. Nevertheless, this may require a more complicated MPPT controller in the PV system.

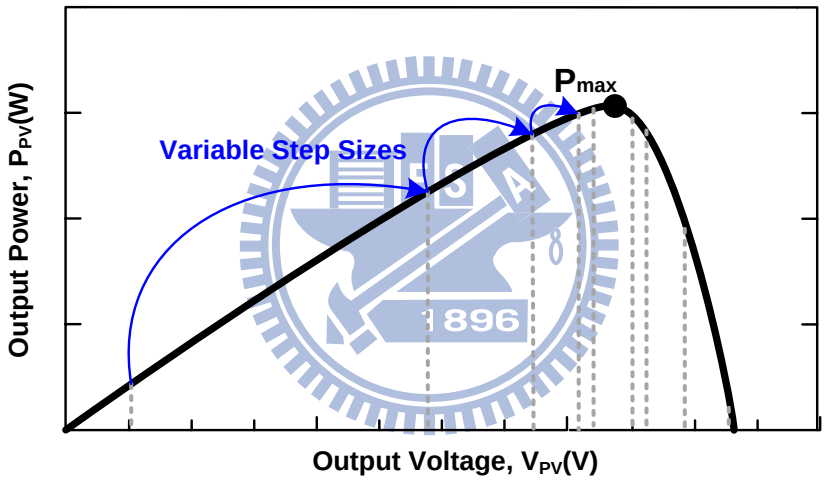

Fig. 3.4. The Perturbation and Observation Tracking Algorithm with Variable Perturbation Step Sizes.

The design complexity of the perturbation and observation tracking technique is higher than the voltage-based method. The MPPT controller needs to calculate the slope at any time instant, which means it requires a lot of arithmetic circuits and the circuits to determine the next perturbation direction. On the other side, the voltage-based tracking algorithm requires only a few circuits to find out the maximum power point from the open-circuit voltage.

To summarize, TABLE 3.1 gives the comparisons between the voltage-based tracking algorithm and the perturbation and observation tracking algorithm in terms of the tracking effectiveness, the tracking speed and the implementation complexity.

TABLE 3.1 Comparisons between Voltage-Base Tracking and Perturbation and Observation Tracking

	Voltage-Based Tracking	**Perturbation and Observation Tracking**
Tracking Accuracy	Worse	Better
Tracking Speed	Faster	Slower
Implementation Complexity	Easier	More complicated

3.3 The Proposed Tracking Algorithm

Fig. 3.5 demonstrates the concept of the proposed MPPT algorithm. Before the solar system turns on, the operating point of the PV system is located on the open-circuit voltage point, V_{OC}. Conventional MPPT algorithm, such as slope detection algorithm [31] [e.g. perturbation/observation (P&O) algorithm or hill-climbing (HC) algorithm] calculates the slope of characteristic power-voltage curve to determine the slope condition and then to track the maximum power point (MPP). Nevertheless, as mentioned before, a PV system adopting this algorithm requires a lengthy amount of time to track the operating point from points V_{OC} to MPP during the system power-on period, as depicted in Fig. 3.5.

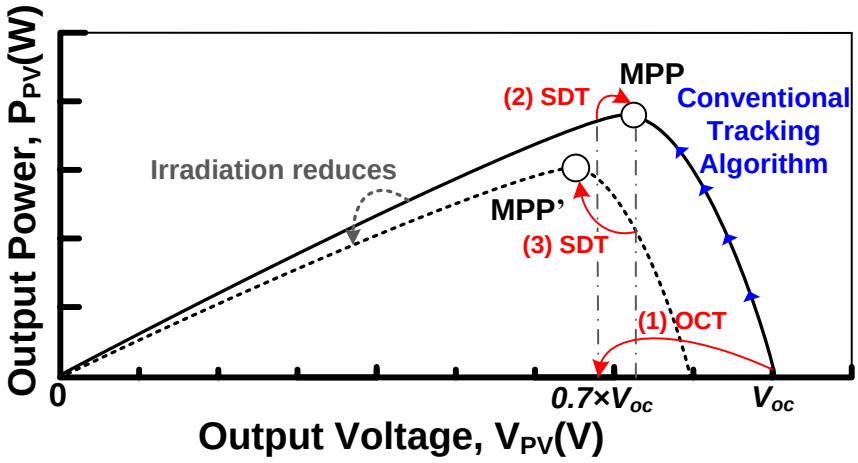

Fig. 3.5. The concept of the proposed MPPT algorithm when irradiation reduces.

Other tracking algorithms such as the constant voltage algorithm use a fixed ratio of maximum power voltage to open-circuit voltage V_{OC} to approximate the MPP. Theoretically, 0.7 fractions of open-circuit voltage V_{OC} is close to the MPP [32]. Therefore, periodically disconnecting the solar array and power stage to measure V_{OC} and multiplying it to 0.7 can rapidly detect the current MPP, as described before. The fraction factor (0.7) varies when different solar cell materials are used. Moreover, it is considerably susceptible to environmental conditions such as ambient temperature and solar irradiation level. In this sense, the MPP cannot be guaranteed when varying environmental conditions are taken into consideration. Moreover, consistent disconnection between the solar array and power stage causes power delivery interruption during the sampling period, thereby resulting in the low power efficiency of the PV system.

To increase both tracking speed and accuracy while maintaining high power efficiency, the open-circuit tracking (OCT) algorithm and the slope detection tracking (SDT) algorithm are both adopted to track the MPP in this study. Disconnection between solar array and the power stage occurs

only one time; that is, in the beginning of the system power-on period. This way, unnecessary power loss can be avoided while maintaining the system power efficiency.

Fig. 3.6 illustrates the timing diagram of the proposed tracking algorithm. E_{slope} is a digital signal used to indicate the slope condition. Logic-high E_{slope} means the slope condition, dP_{PV}/dV_{PV}, of the solar panel is positive. On the contrary, logic-low E_{slope} means dP_{PV}/dV_{PV} is negative. The signal *OCT Enable* indicates whether the OCT tracking algorithm is enabled or not. The signal V_G is the gate signal of the power NMOS in the boost converter. The signal I_{L1} shows the inductor current of the boost converter, which can also indicate the current of the solar panel.

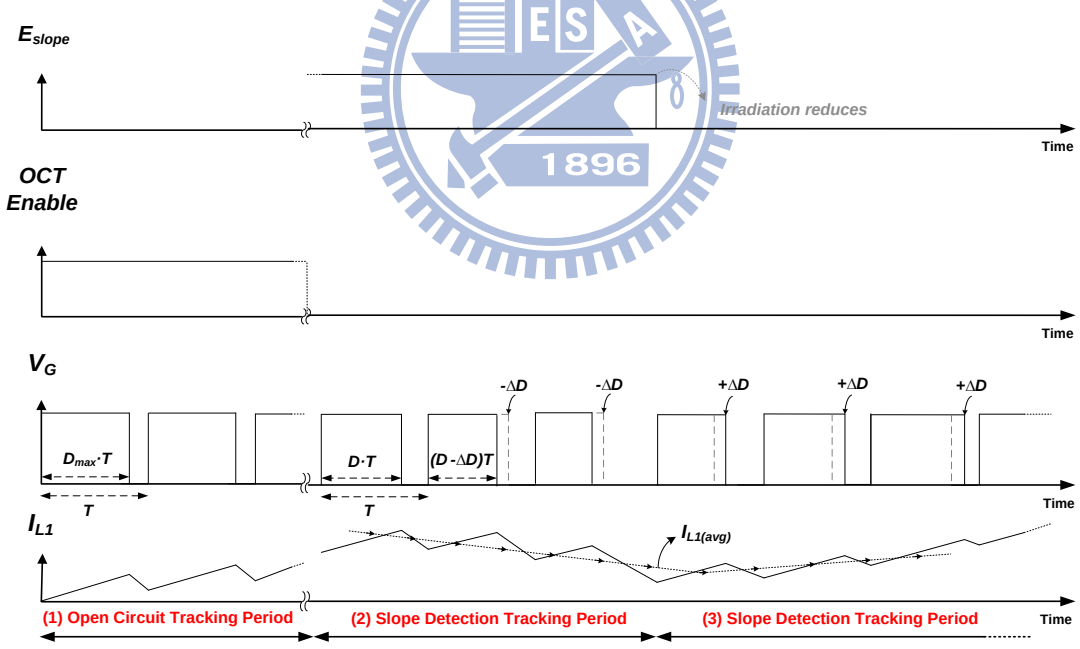

Fig. 3.6. The timing diagram of the proposed MPP tracking algorithm.

Basically, the tracking procedure can be divided into the following sequences.

The first step is: Before the solar system turns on, V_{OC} is detected by the controller to set the PV panel voltage, V_{PV}, close to $0.7 \times V_{OC}$ for improving the tracking speed compared to the disadvantage of slow tracking speed in the conventional P&O and HC algorithms. Besides, the switching duty cycle of the boost converter is set to its maximum value in order to accelerate the tracking speed during the open-circuit voltage detection period.

The second step is: the SDT technique takes over the tracking procedure to continually and accurately track the MPP to make sure that the power stage receives the most energy from the solar panel.

The third step is: If the environmental condition changes, say, the irradiation level reduces, the slope condition changes from positive to negative, according to the solar cell characteristic shown in Fig. 3.1. Then, E_{slope} transits from high to low. Aforementioned in Section 2.1, the voltage is inversely proportional to the current. As a result, the SDT technique will increase the switching duty cycle. The current of solar array, therefore, increases to pull down the operating voltage and ensures the system operating move to a new maximum power point, *MPP'*, as illustrated in Fig. 3.5.

On the other hand, if the environmental temperature reduces, as shown in Fig. 3.7, the new maximum power point, *MPP'*, is higher than the old one, *MPP*. The PV system can still locate the new maximum power point through the proposed algorithm and then work on this new operating point.

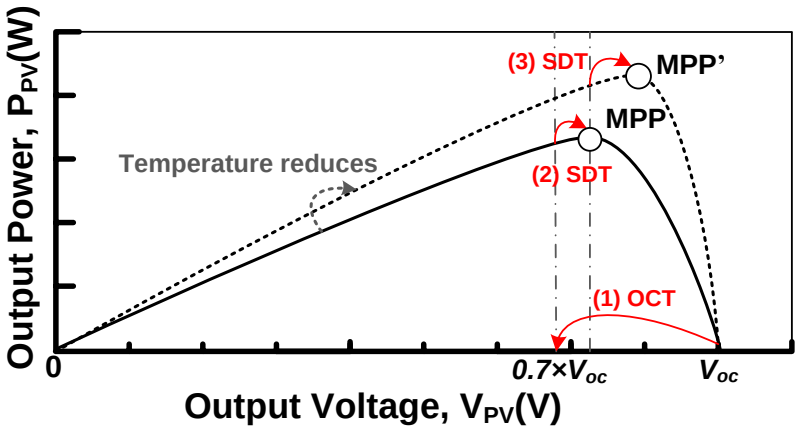

Fig. 3.7. The concept of the proposed MPPT algorithm when temperature reduces.

The flowchart in Fig. 3.8 summarizes the overall tracking topology of the proposed MPP tracking algorithm. After the solar system turns on, the OCT technique is enabled until the operating voltage is set to be around $0.7\times V_{OC}$. After that, the SDT technique consistently monitors the slope condition and makes sure the system operate at MPP regardless of any condition change in the environment. When the signal E_{slope} is set to be logic high, this may mean the irradiation level increases or the temperature reduces, the controller will decrease the switching duty cycle to the boost converter in order to pull down the inductor current. Meanwhile, the PV current is reduced as well and the PV voltage is increased conversely, which forces the system to operate toward the MPP. On the other hand, if the signal E_{slope} is detected to be logic low, the inductor current and the PV current is raised by the increased duty ratio. Therefore, the PV voltage is pulled down to track the MPP.

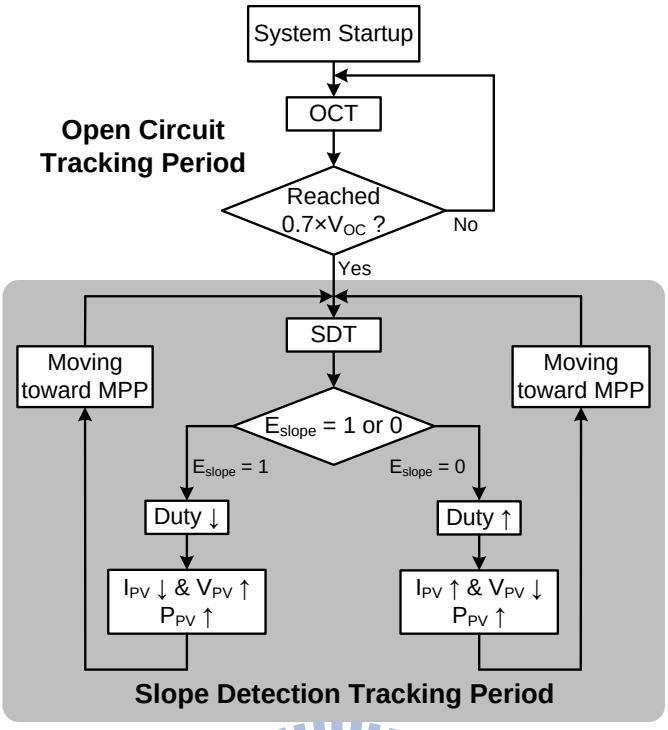

Fig. 3.8. The flowchart of the proposed MPP tracking algorithm.

The proposed AMPPT technique includes both the advantages of the OCT technique and the SDT technique. That is, the OCT technique can rapidly but roughly locate the MPP with fast tracking speed. In the meanwhile, the SDT technique improves the tracking accuracy which cannot be guaranteed by the OCT technique.

3.4 Shading Effect and Global MPPT Algorithm

For a large scale photovoltaic system, unavoidable shadow from the nearby trees, cloud and buildings frequently cause the energy degradation of the solar array. The so called “partial shading effect” [33] poses a great threat to highly efficient utilization of the PV system. As depicted in Fig. 3.9, when the solar arrays are shaded, there exists more than one local

maximum power point. As a result, the designed MPP tracker may easily misjudge the optimal operating point and therefore the system cannot provide its maximum energy. The proposed MPP tracking algorithm in this paper can be further improved by the algorithm provided in Fig. 3.10 to ensure the robustness of the PV system.

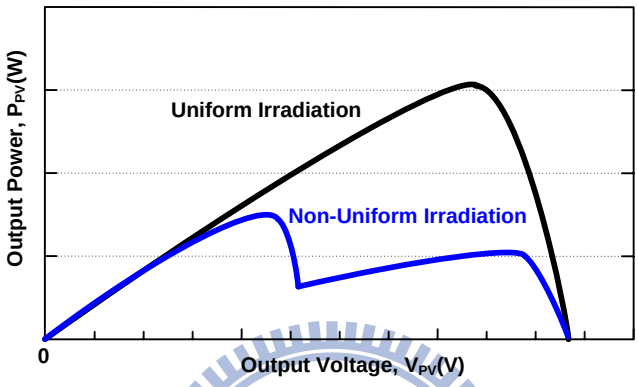

Fig. 3.9. P-V Characteristic Curve due to non-uniform irradiation level.

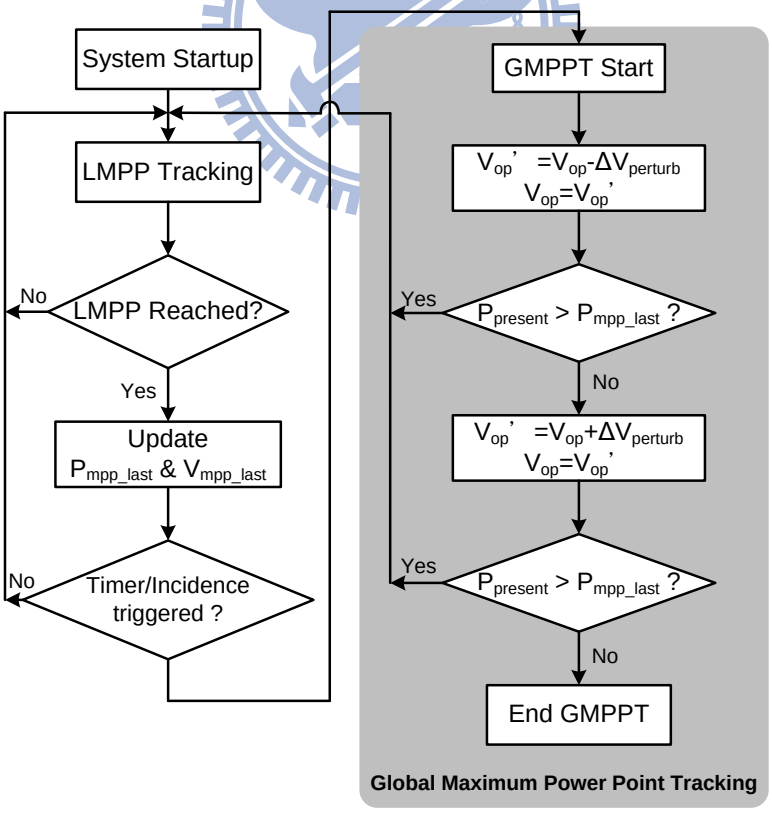

Fig. 3.10. Flow chart of the global maximum power point tracking.

The system primarily determines whether it has reached its local maximum power point (*LMPP*). The measured power (P_{mpp_last}) and voltage (V_{mpp_last}) are then stored for later comparison. The control loop enters the global maximum power point tracking (GMPPT) stage when triggered by the timer. The default timer is set to 1 s. That is, the global maximum power point (GMPP) tracker is enabled every second to check whether the current operating point belongs to the GMPP. If the current operating point is already the maximum point on the power-voltage plane, the system will continuously operate at this point. Otherwise, the GMPP tracker locates the GMPP and forces the system to operate on the located point. During the GMPPT stage, the system is perturbed by a voltage difference $\Delta V_{perturb}$, which is approximated to 60%–70% of V_{oc} [34], as sketched in Fig. 3.11. Thus, an MPPT technique guarantees full robustness of the connected PV system.

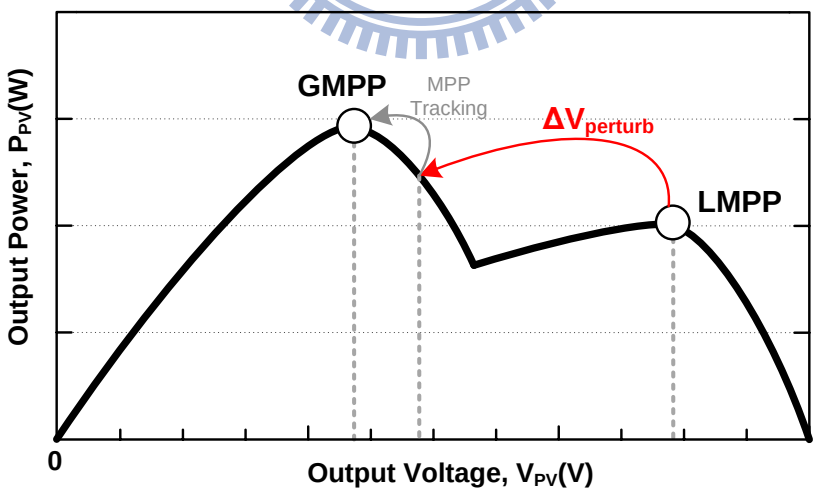

Fig. 3.11. P-V characteristic curve sketching the tracking of the global maximum power point due to non-uniform irradiation level.

Chapter 4

The Proposed Circuit of the MPPT Controller

4.1. Maximum Power Point Tracker Interface Topologies

This chapter provides a comparative study with a goal of choosing the suitable converter topology for the application of maximum power point tracking in a PV system. Both the DC-DC buck converter and the DC-DC boost converter are usually used in the PV power system because of their simplicity and efficiency. The following paragraphs analyze both of these converter topologies and draw a conclusion of choosing the appropriate one for the maximum power point tracker in a PV system.

4.1.1. The Basic Working Principles of Buck Converter

Fig. 4.1 shows a schematic of a conventional DC-DC buck converter connected to a solar array. It comprises of a solar array as the power source, input and output capacitor, C_1 and C_2, respectively. A switch S and a diode D are also presented in the figure. R_{out} is the summarized loading of the next stage, which is the DC-AC inverter in the proposed PV application.

Under the condition of continuous current mode, the operation of buck converter can be divided into two phases. In phase 1, as shown in Fig. 4.2, the switch S is turned on, which means it creates a short-circuit path

between the input node V_{pv} and the output node V_{bus} through the switch S and the inductor L. The energy from the solar array is then charging the inductor L and providing the energy for the output node V_{bus}. The timing diagram is depicted in Fig. 4.4. The symbol d represents the duty cycle to the switch. T_s is the switching period of the converter and V_{C2} is the voltage across the output capacitor C_2, which equals to the output voltage V_{bus}. During this phase, the inductor current is increasing with the time and the voltage across the inductor is V_{pv}-V_{bus}, assuming the switch is ideal.

Phase 2 happens when the switch S is turned off. At this time, the diode D is conducted to form a path from the ground to the output node V_{bus}, as shown in Fig. 4.3. The solar array is disconnected from the inductor since the switch S is turned off, which means it no longer supplies solar energy for the output node. Instead, the energy stored on inductor L provides the need for the loading. As a result, the inductor waveform in phase 2 is decreasing with the time. The voltage across the inductor is $-V_{bus}$, assuming the diode D is ideal.

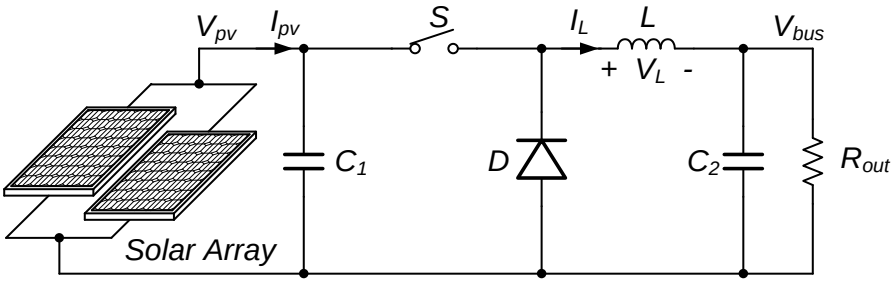

Fig. 4.1 Schematic of a buck converter.

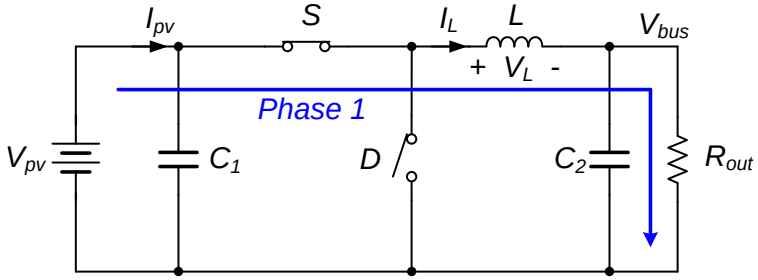

Fig. 4.2 The buck converter during phase 1.

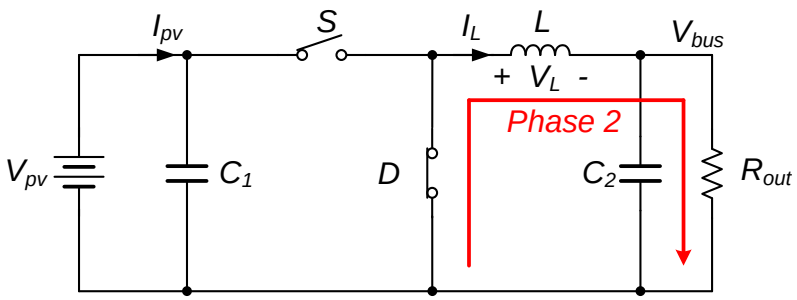

Fig. 4.3 The buck converter during phase 2.

The voltage across the inductor at any time can be calculated as Eq. (4.1).

$$V_L = L\frac{dI_L}{dt} \tag{4.1}$$

$$\frac{dI_L}{dt} = \frac{V_L}{L} \tag{4.2}$$

As a result, the slope of inductor current during the rising period can be calculated as

$$m_1 = \frac{V_{pv} - V_{bus}}{L} \tag{4.3}$$

And the slope of the inductor current during the decreasing period can be given as

$$m_2 = \frac{-V_{bus}}{L} \tag{4.4}$$

The average inductor voltage is zero over a full switching period T_s, with that Eq. (4.5) ~ Eq. (4.7) can be derived.

$$m_1 \cdot dT_s + m_2 \cdot (1-d)T_s = 0 \tag{4.5}$$

$$\frac{V_{pv} - V_{bus}}{L} \cdot dT_s + \frac{-V_{bus}}{L} \cdot (1-d)T_s = 0 \tag{4.6}$$

$$V_{bus} = d \cdot V_{pv} \tag{4.7}$$

Duty ratio d is a value between 0 and 1, therefore, Eq. (4.7) verifies that the buck converter lower the input voltage to the output voltage.

The inductor current ripple Δi_L can be decided from the following equations.

$$2\Delta i_L = m_1 \cdot dT_s = \frac{V_{pv} - V_{bus}}{L} \cdot dT_s \tag{4.8}$$

$$\Delta i_L = \frac{V_{pv} - V_{bus}}{2L} \cdot dT_s \tag{4.9}$$

Assuming that the stored charge from the inductor transfers completely to the output capacitor without any lose, which means

$$\Delta Q = C_2 \cdot 2\Delta v_{C2} \tag{4.10}$$

Then, the voltage ripple ΔV_{C2} on the output node can be calculated as the following equations.

$$\Delta Q = \frac{1}{2} \cdot \Delta i_L \cdot \frac{1}{2} T_s = \frac{1}{4} \Delta i_L T_s \tag{4.11}$$

$$2\Delta v_{C2} = \frac{\Delta Q}{C_2} = \frac{\frac{1}{4} \Delta i_L T_s}{C_2} \tag{4.12}$$

$$\Delta v_{C2} = \frac{\Delta i_L T_s}{8 C_2} \tag{4.13}$$

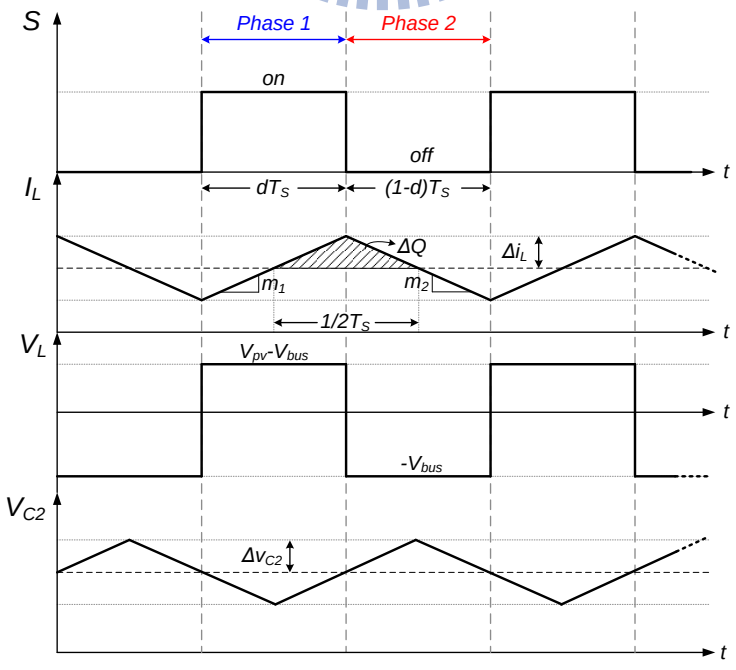

Fig. 4.4 The timing diagram of buck converter.

4.1.2. The Basic Working Principles of Boost Converter

Fig. 4.5 shows a schematic of a conventional DC-DC boost converter connected to a solar array. The solar array serves as the power source to the converter. The boost converter also consists of an input capacitor and an output capacitor, C_1 and C_2, respectively. The switch S turns on and off periodically to regulate the output voltage. A diode D is also presented in the figure. R_{out} is the summarized loading of the next stage, which is the DC-AC inverter in the proposed PV application.

Under the condition of continuous current mode, the operation of boost converter can be divided into two phases like the buck converter. In phase 1, as shown in Fig. 4.6, the switch S is turned on, which means it creates a short-circuit path between the input node V_{pv} and the ground through the switch S and the inductor L. The energy from the solar array is then charging the inductor L through this path. Since the output node is disconnected to the solar array, the output power is dependent on the energy stored on the output capacitor C_2. The timing diagram is shown in Fig. 4.8. The symbol d represents the duty cycle to the switch S. T_s is the switching period of the converter and V_{C2} is the voltage across the output capacitor C_2, which equals to the output voltage V_{bus}. During this phase, the inductor current is increasing with the time and the voltage across the inductor is V_{pv}, if the switch is assumed to be ideal.

When the switch S is turned off, the boost converter enters phase 2. At this time, the diode D is conducted to form a path from the solar array to the output node V_{bus}, as shown in Fig. 4.7. The energy from the solar array is then transferring to the output node. Because the output voltage V_{bus} is

higher than the input voltage V_{pv}, the inductor waveform in phase 2 is decreasing with the time. The voltage across the inductor is V_{pv}–V_{bus}, assuming the diode D is ideal.

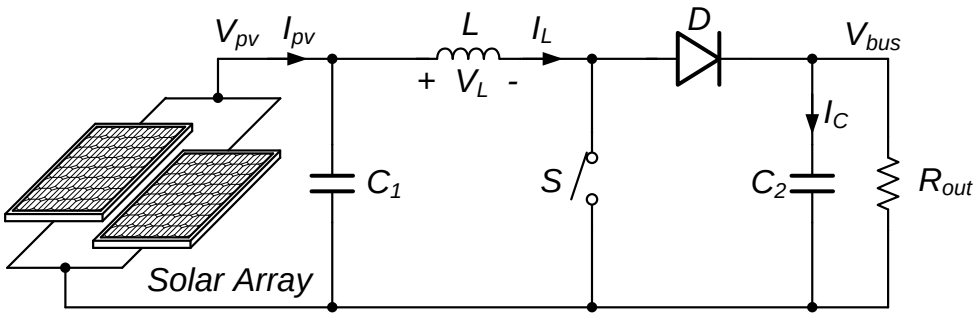

Fig. 4.5 Schematic of a boost converter.

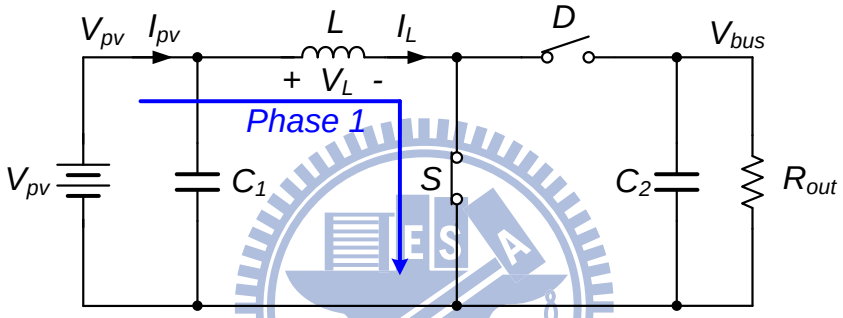

Fig. 4.6 The boost converter during phase 1.

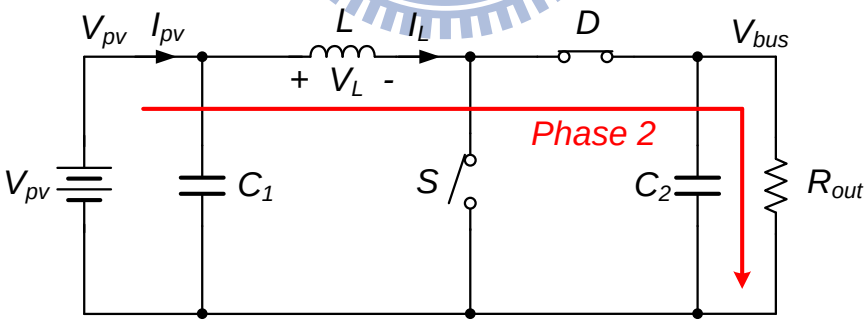

Fig. 4.7 The boost converter during phase 1.

From Eq. (4.1) and Eq. (4.2), the slope of inductor current m_1 during phase 1 can be calculated as

$$m_1 = \frac{V_{pv}}{L} \tag{4.14}$$

And the slope of the inductor current m_2 during the decreasing period,

namely phase 2, can be given as

$$m_2 = \frac{V_{pv} - V_{bus}}{L} \tag{4.15}$$

Again, as aforementioned in the buck converter, the average inductor voltage of the boost converter is also zero over a full switching period T_s. According to Eq. (4.5), Eq. (4.16) and Eq. (4.17) can be derived.

$$\frac{V_{pv}}{L} \cdot dT_s + \frac{V_{pv} - V_{bus}}{L} \cdot (1-d)T_s = 0 \tag{4.16}$$

$$V_{bus} = \frac{1}{1-d} V_{pv} \tag{4.17}$$

Contrarily to the buck converter, Eq. (4.17) shows that the boost converter can increase the input voltage to a higher output voltage since the duty ratio d is a value between 0 and 1.

The inductor current ripple Δi_L can be decided from the following equations.

$$2\Delta i_L = m_1 \cdot dT_s = \frac{V_{pv}}{L} \cdot dT_s \tag{4.18}$$

$$\Delta i_L = \frac{V_{pv}}{2L} \cdot dT_s \tag{4.19}$$

The current flowing through a capacitor can be shown as Eq. (4.20).

$$I_C = C\frac{dV_C}{dt} \tag{4.20}$$

Therefore, the capacitor voltage slope can be derived as

$$\frac{dV_C}{dt} = \frac{I_C}{C} \tag{4.21}$$

The current flowing through the output capacitor C_2 during phase 1 is in a negative direction, which means the current I_C in phase 1 is

$$I_C = -\frac{V_{bus}}{R_{out}} \tag{4.21}$$

On the other hand, during phase 2, the inductor current I_L flows through both the output capacitor C_2 and the output load R_{out}. As a

consequence, the capacitor current I_C equals to Eq. (4.22).

$$I_C = I_L - \frac{V_{bus}}{R_{out}} \tag{4.22}$$

According Eq. (4.21), the capacitor voltage slope of a boost converter during phase 1 and phase 2 are Eq. (4.23) and Eq. (4.24), respectively.

$$m_3 = \frac{I_C}{C_2} = -\frac{V_{bus}}{R_{out}C_2} \tag{4.23}$$

$$m_4 = \frac{I_C}{C_2} = \frac{I_L}{C_2} - \frac{V_{bus}}{R_{out}C_2} \tag{4.24}$$

Change in output capacitor voltage during phase 1 can be shown as

$$-2\Delta v_{C2} = m_3 \cdot dT_s = -\frac{V_{bus}}{R_{out}C_2} dT_s \tag{4.25}$$

Hence, the output voltage ripple of a boost converter is as Eq. (4.26).

$$\Delta v_{C2} = \frac{V_{bus}}{2R_{out}C_2} dT_s \tag{4.26}$$

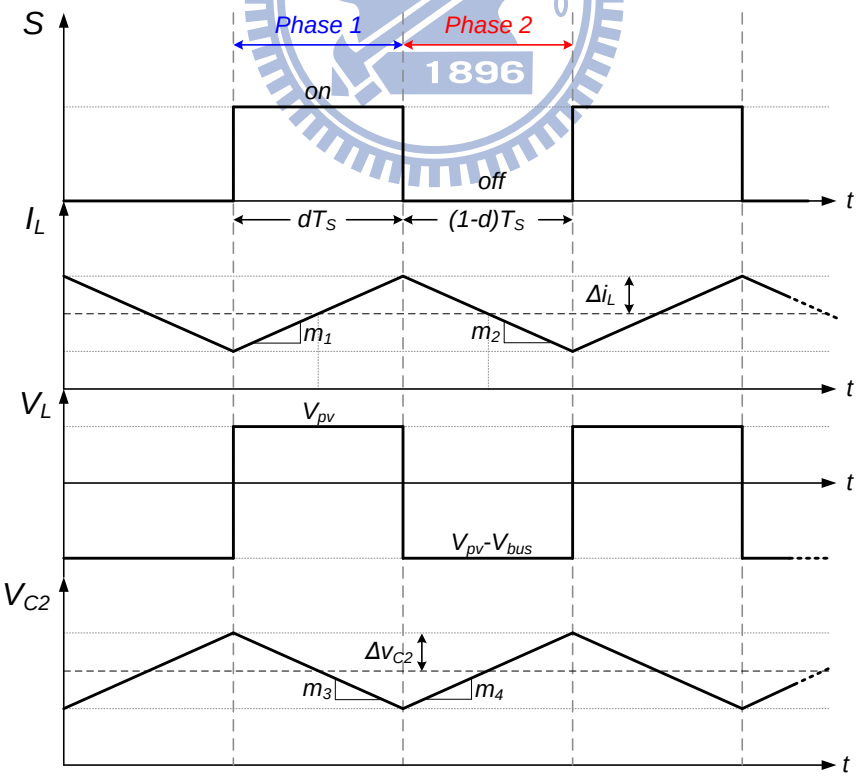

Fig. 4.8 The timing diagram of boost converter.

4.1.3. Converter Topology Selection for MPP Tracker

Considering the working principles of both the buck and boost converter, the boost topology has some advantages over the buck counterpart for the PV application, which are discussed in the following.

The boost converter has a continuous input current; on the contrary, the buck converter exhibits a discontinuous input current. This makes the buck topology require a large and expensive capacitor to smooth the discontinuous input current from the solar array and to handle significant current ripple. On the other hand, the photovoltaic current in the boost converter is as smooth as its inductor current, without any input capacitor. A small and cheap capacitor can further smooth the photovoltaic current and voltage for the boost converter.

For the selection of the power MOSFETs and driver, as shown in [35], the boost converter requires a lower current rating power MOSFET compared to the one used in a buck converter. The buck converter also needs a high-side MOSFET driver, which is more complex and expensive than the low-side driver used in the boost converter.

In most applications, the photovoltaic array acts as a power source to energize devices capable of storing electricity and a power grid. However, the capacity of solar generation systems depends heavily on the presence of light. At night, a current could flow back into solar arrays from the bus. This reverse current has to be prevented because it causes loss, extensive damage, or could even cause a fire [36]. Blocking diode is an effective way to avoid reverse current. In the selection of blocking diodes, the boost topology shows significant advantages over the buck converter. In the boost

converter, the freewheel diode can serve as the blocking diode to avoid reverse current. However, in the buck topology, the blocking diode is an additional component that is needed to conduct the full photovoltaic current. This results in an increase in cost and additional power loss due to the forward voltage drop on the blocking diode.

In summary, considering the advantages of the boost converter over its buck counterpart when used as a maximum power point tracker in a PV system, this study chooses the boost converter as the interface for tracking the maximum power point.

4.2. Maximum Power Point Formula and Slope Calculation

For the purpose of tracking the maximum power point at any time instant, the PV system needs to constantly calculate the slope condition of the solar array's characteristic curves. With the information of the slope condition, the MPP tracker can consequently find the maximum power point and then force the system to operate on this maximum power point. The following shows the formula used to calculate the maximum power point and its slope detection circuits.

To find the maximum power point, one needs to find the location where the slope is zero or close to zero on the power-voltage characteristic curve, as shown in Fig. 4.9.

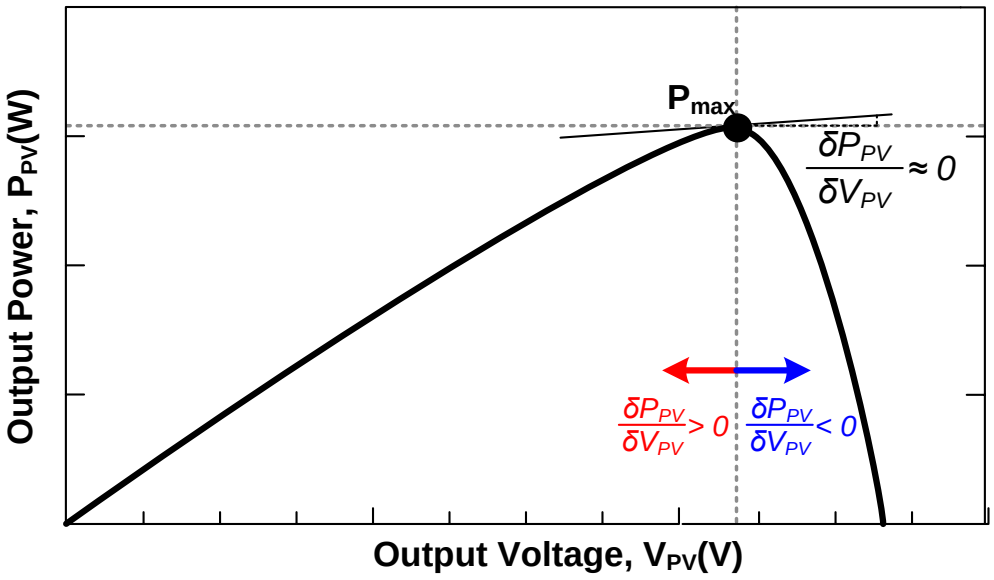

Fig. 4.9 The maximum power point on the power-voltage characteristic curve.

That means the slope equation holds

$$\frac{\partial P_{PV}}{\partial V_{PV}} \approx 0 \tag{4.27}$$

on the maximum power point or near it.

The slope equation, Eq. (4.27), according to the characteristic curves of power-voltage can be written as Eq. (4.28).

$$\begin{aligned}
\frac{\partial P_{PV}}{\partial V_{PV}} &= \frac{\partial \left(V_{PV} \cdot I_{PV} \right)}{\partial V_{PV}} \\
&= \frac{\partial V_{PV}}{\partial V_{PV}} \cdot I_{PV} + V_{PV} \cdot \frac{\partial I_{PV}}{\partial V_{PV}} \\
&= I_{PV1} + V_{PV1} \cdot \frac{I_{PV2} - I_{PV1}}{V_{PV2} - V_{PV1}} \\
&= I_{PV1} - V_{PV1} \cdot \frac{I_{PV1} - I_{PV2}}{V_{PV2} - V_{PV1}} \\
&= I_{PV1} - V_{PV1} \cdot \frac{\Delta I_{PV}}{\Delta V_{PV}}
\end{aligned} \tag{4.28}$$

The denominator in Eq. (4.28) is eliminated deliberately by the conversion ratio of the voltage-to-current (V-to-I) converter to improve the accuracy of the slope detection circuit.

The slope detector detects the voltage and current information at two different time instances: (I_{PV1}, V_{PV1}) at time t_1 and (I_{PV2}, V_{PV2}) at time t_2. Using the sample-and-hold circuit to detect the voltage and current of the solar array, V_{PV1} and I_{PV1} represent the instant voltage and current of the solar array, respectively. Similarly, V_{PV2} and I_{PV2} record the previous voltage and current, respectively.

The voltage difference between two sampling times is set as a fixed PV difference voltage $\Delta V_{PV(fixed)}$. V_{PV1} is also converted to current signal I_{VPV1} by the V-to-I converter for easy and fast operation in analog circuits. As a result, the operation of the divider can simply be substituted by parameter k, as shown in the following equation:

$$\frac{\partial P_{PV}}{\partial V_{PV}} = I_{PV1} - k \cdot I_{VPV1} \cdot \Delta I_{PV} \qquad (4.29)$$

$$where \qquad k = \frac{V_{PV1}}{\Delta V_{PV(fixed)}}$$

The current difference, ΔI_{PV}, between I_{PV1} and I_{PV2}, can be derived by the current subtractor. Moreover, the multiplication of I_{VPV1} and ΔI_{PV}, can be achieved by the wide-range current multiplier proposed in this thesis.

It's obvious from Fig. 4.9 that the maximum power point occurs at the point where the slope is zero or near to zero. Therefore, one can try to find an operating point whose slope is as low as possible, no matter it is negative or positive. Once this point is found, the maximum power point can then be

decided.

Nevertheless, there is a simpler way to do the tracking. Observing the characteristic PV curve of solar array in Fig. 4.9, the maximum power point situates between the right-hand side plane and the left-hand side plane of the curve. Namely, the maximum power point occurs on the slope transition point, where slope changes from either positive to negative or negative to positive. Comparing the current I_{PV1} and $k\times(I_{VPV1}\times\Delta I_{PV})$ in Eq. (4.29), therefore, one can determine the slope condition of solar panel, which can be easily carried out by a current comparator.

4.3. Slope Detection Circuit

Fig. 4.10 shows the block diagram of the proposed slope detection circuit following Eq. (4.29). The slope detection circuit includes a current subtractor, a voltage-to-current converter, a current comparator, and a wide-range current multiplier. The current subtractor serves the purpose of computing the current difference between I_{PV1} and I_{PV2}. The output current of the current subtractor is ΔI_{PV}. The voltage-to-current converter is used to convert the voltage data V_{PV1} into the current data I_{VPV1} for further calculation need. The wide-range current multiplier multiplies both ΔI_{PV} and I_{VPV1}. In the end, the current comparator compares I_{PV1} and $k\times(I_{VPV1}\times\Delta I_{PV})$ to judge the slope condition and sends out a digital signal, either high or low, to indicate the slope condition at that time instant.

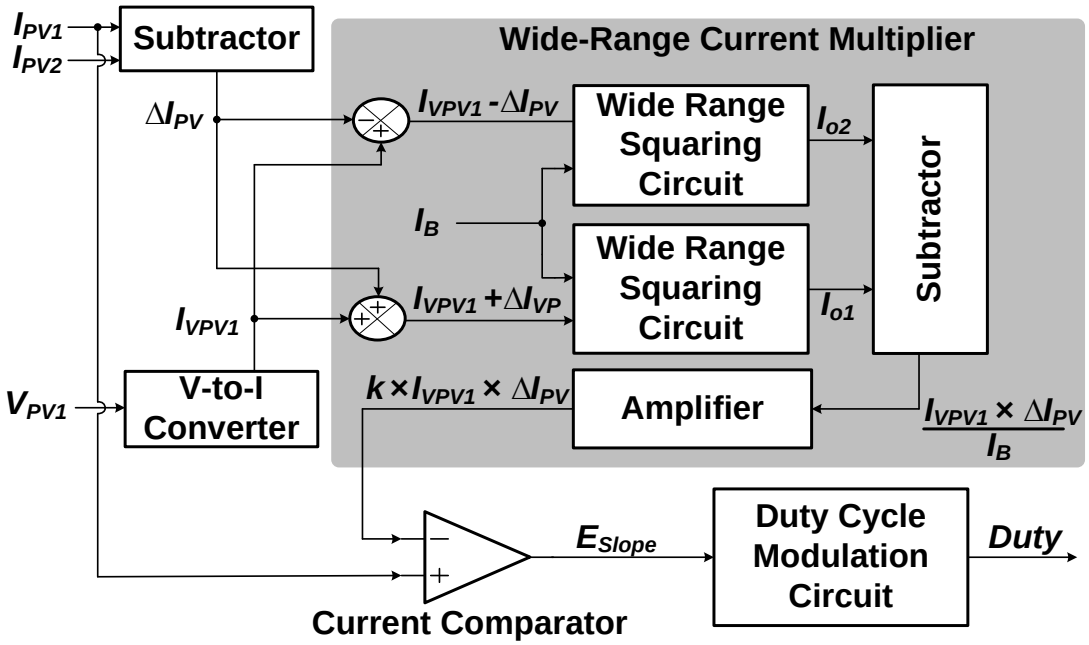

Fig. 4.10 The proposed slope detection circuit.

The digital signal E_{slope} indicates the slope condition for the duty cycle modulation circuit, which is implemented by a 7-bit up-down counter. The duty cycle modulation circuit increases or decreases the duty cycle of the boost converter. As mentioned in Chapter 2, the voltage and current of solar panel are inversely proportional to each other. When the slope is positive, the value of E_{slope} is high to decrease the duty cycle of the converter and thus increase the operating voltage. On the other hand, a low value of the E_{slope} indicates the slope is negative. Then the duty cycle increases to decrease the operating voltage.

Since the characteristic of solar array follows majorly the environmental factors, such as the temperature and the irradiation, the voltage and current range of solar panel are very wide. As a result, typical current multipliers barely meet the need in the PV application.

As can be seen in Fig. 4.10, the proposed wide-range current

multiplier is composed of the wide-range squaring circuit, current subtractor and amplifier. The proposed wide-range squaring circuit in the wide-range current multiplier consists of a high current (HI) processor and a low current (LI) processor. This wide-range squaring circuit serves the purpose of extending the allowable current range of the current multiplier. Fig. 4.11 shows the transistor level schematic of the wide-range current squaring circuit. All the current mirrors are implemented in the cascade way to improve the calculation accuracy. The current comparator in the figure decides whether the input current, $I_{VPV1}+\Delta I_{PV}$, is larger or smaller than the reference current, I_{ref}. If ($I_{VPV1}+\Delta I_{PV}$) is larger than I_{ref}, the HI processor is activated and the current ($I_{VPV1}+\Delta I_{PV}$) flows into the drain terminal of MOSFET M_{HI3}. After that, the current mirror produces current equal to $2\times(I_{VPV1}+\Delta I_{PV})$ flowing out from the source terminal of M_{HI3}. By Kirchhoff's Voltage Law (KVL), the summation of $V_{GS,MHI1}$ and $V_{GS,MHI3}$ is equal to that of $V_{GS,MHI2}$ and $V_{GS,MHI4}$ as expressed in Eq. (4.30).

$$V_{GS,MHI1}+V_{GS,MHI3}=V_{GS,MHI2}+V_{GS,MHI4} \tag{4.30}$$

The squaring principle of MOSFET gives

$$I_{DS}=K\left(V_{GS}-V_t\right)^2 \tag{4.31}$$

$$V_{GS}=V_t+\sqrt{\frac{I_{DS}}{K}} \tag{4.32}$$

where $K=\frac{1}{2}\mu_0 C_{ox}\frac{W}{L}$ denotes the transconductance parameter of transistor, I_{DS} is the current flowing through the transistor, V_{GS} is the voltage between gate and source, and V_t is the threshold voltage of the transistor.

Based on squaring principle of transistor in Eq. (4.32), the following equation can be derived from Eq. (4.30).

$$\left(V_t+\sqrt{\frac{I_{MHI1}}{K}}\right)+\left(V_t+\sqrt{\frac{I_{MHI3}}{K}}\right)=\left(V_t+\sqrt{\frac{I_{MHI2}}{K}}\right)+\left(V_t+\sqrt{\frac{I_{MHI4}}{K}}\right) \tag{4.32}$$

$$\sqrt{I_{MHI1}}+\sqrt{I_{MHI3}}=\sqrt{I_{MHI2}}+\sqrt{I_{MHI4}} \tag{4.32}$$

Furthermore, by Kirchhoff's Current Law (KCL), the following equations can be derived.

$$I_{MHI3}=I_{o1}+\left(I_{VPV1}+\Delta I_{PV}\right) \tag{4.33}$$

$$I_{MHI1}=I_{o1}-\left(I_{VPV1}+\Delta I_{PV}\right) \tag{4.34}$$

$$I_{MHI2}=I_{MHI4}=I_B \tag{4.35}$$

I_B stands for the bias current in the squaring circuit. Substituting Eq. (4.33), Eq. (4.34) and Eq. (4.35) into Eq. (4.32),

$$\sqrt{I_{o1}-\left(I_{VPV1}+\Delta I_{PV}\right)}+\sqrt{I_{o1}+\left(I_{VPV1}+\Delta I_{PV}\right)}=\sqrt{I_B}+\sqrt{I_B} \tag{4.36}$$

Squaring both sides, one can derive

$$4I_B=\left(I_{VPV1}+\Delta I_{PV}\right)+I_{o1}+I_{o1}-\left(I_{VPV1}+\Delta I_{PV}\right)+2\sqrt{I_{o1}^2-\left(I_{VPV1}+\Delta I_{PV}\right)^2} \tag{4.37}$$

Eliminating ($I_{VPV1}+\Delta I_{PV}$) and squaring both sides again,

$$16I_B^2-16I_BI_{o1}+4I_{o1}^2=4I_{o1}^2-4\left(I_{VPV1}+\Delta I_{PV}\right)^2 \tag{4.38}$$

Then, the following equation can be derived.

$$I_{o1}=\frac{\left(I_{VPV1}+\Delta I_{PV}\right)^2}{4I_B}+I_B \tag{4.39}$$

Likewise, another identical wide-range squaring circuit can derive I_{o2} in Fig. 4.11, where the input current is (I_{VPV1}-ΔI_{PV}), as shown in Eq. (4.40).

$$I_{o2} = \frac{\left(I_{VPV1} - \Delta I_{PV}\right)^2}{4I_B} + I_B \tag{4.40}$$

Subtracting I_{o2} from I_{o1}, $k\times(I_{VPV1}\times\Delta I_{PV})$ can be obtained by amplifying the current $(I_{VPV1}\times\Delta I_{PV})/I_B$. E_{slope} is generated in the end to adjust the duty cycle of the boost converter. Accordingly, the operating voltage of solar array is ensured to locate at the maximum power point.

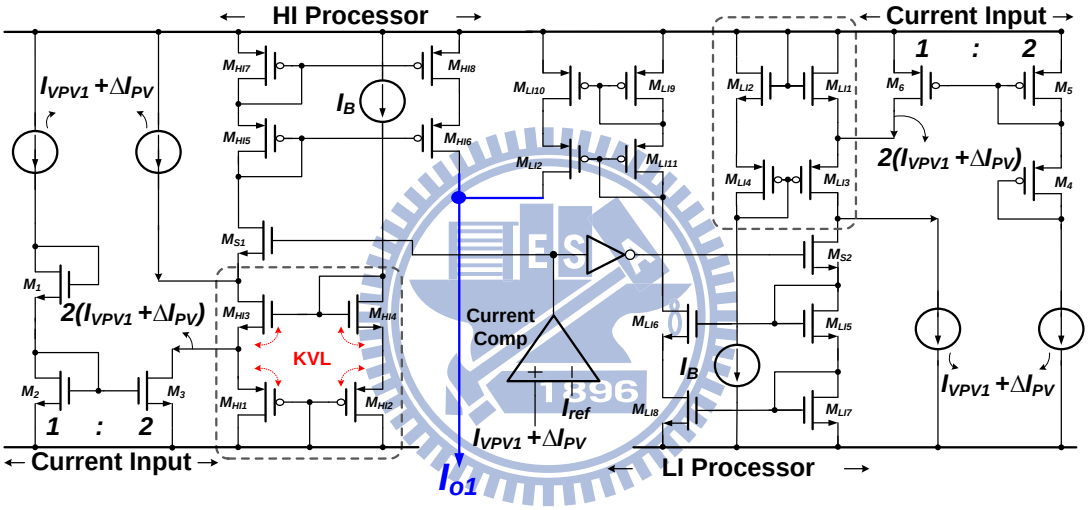

Fig. 4.11 The proposed wide-range squaring circuit.

The proposed wide range squaring circuit and the slope detection circuit can precisely determine the slope condition at any instant and under any circumstance. The boost converter and other controlling circuits in the controller, then, use the detected slope information to manipulate the operating point of the PV system. For that, the PV system can continuously operate under maximum power condition and with high power conversion ratio.

Chapter 5

Simulation and Experiment Results

5.1 Simulation Results

5.1.1 PSIM Simulations

To verify the proposed maximum power point tracking algorithm and the overall PV system, PSIM simulation, for its simplicity and effectiveness, is used in the beginning. First of all, the nonlinear characteristic of the solar array has to be created to supply the necessary information for either the maximum power point tracker or the power converter stage. The characteristics of the solar array, however, are hard to predict and as a result the necessary parameters are also difficult to be identified. Eq. (5.1) revisits the formula discussed before. It reveals that the parameters mainly depend on the irradiation level and the ambient temperature.

$$I_{PV} = I_L - I_{os}\left\{\exp\left[\frac{q}{AkT}\left(V_{PV} + I_{PV}R_s\right)\right] - 1\right\} - \frac{V_{PV} + I_{PV}R_s}{R_P} \tag{5.1}$$

The next step is to determine the relationship between the parameters, I_L, I_{OS}, R_S, R_P, etc., the irradiation and the temperature. Referring to the parameters given in [37] and establishing the relationship to the irradiation and temperature, one can rephrase Eq. (5.1) into Eq. (5.2).

$$\begin{aligned} I_{PV} = {} & \left(13.25 - 0.033T + 6.96\times10^{-3}S\right) \\ & - 6.5\times10^{-6}\left(\exp\left(\frac{V_{PV}}{\left(67.52 - 0.336T + 0.018S\right)\left(8.63\times10^{-5}(T+273)\right)}\right) - 1\right) \\ & - \left(\frac{V_{PV}}{617.6 - 3.4T + 0.638S}\right) \end{aligned} \tag{5.2}$$

In Eq. (5.2), the relationship between photovoltaic current, $I_{PV,}$

photovoltaic voltage, V_{PV}, the irradiation level, S, and the ambient temperature, T, is established. The PV current and PV voltage are obviously dependent on both the irradiation and the temperature. Fig. 5.1 shows the PSIM schematic for the PV array simulation under the condition of different irradiation levels. Eq. (5.2) is used here as a function block *m* to provide the transfer function for I_{PV}.

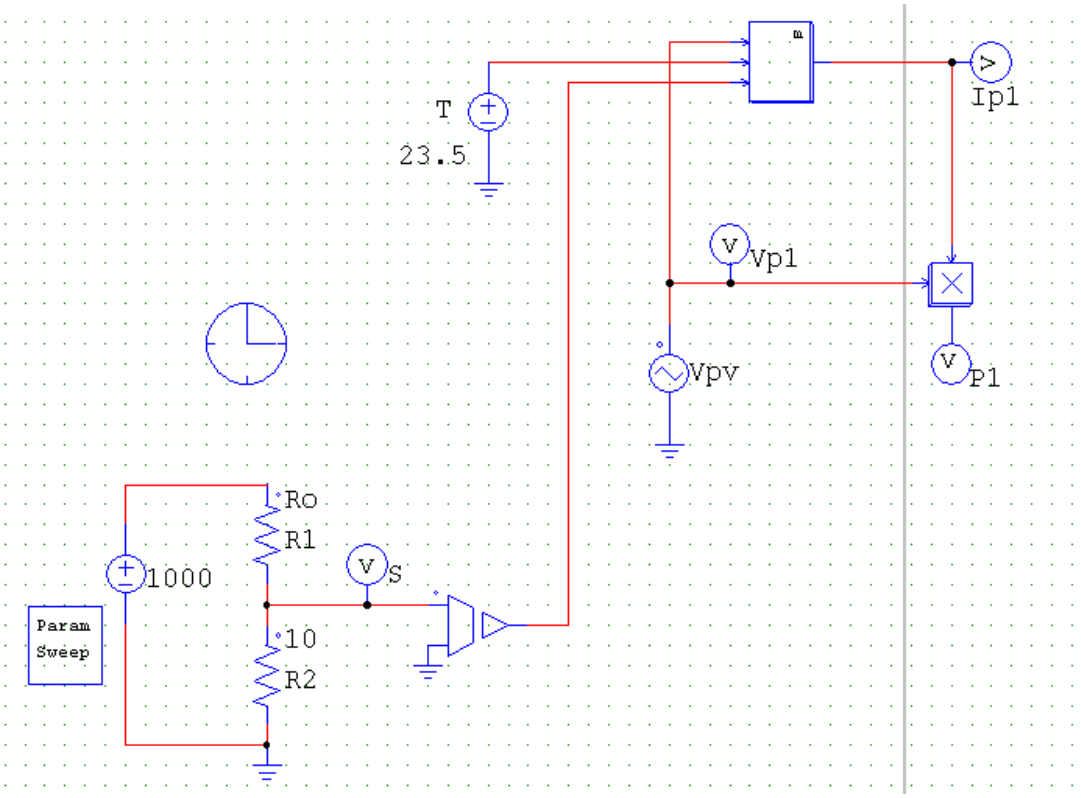

Fig. 5.1 PSIM schematic of PV array with different solar irradiation levels.

Fig. 5.2 and Fig. 5.3 show the simulation results under different irradiation levels according to PV current and PV power respectively. Fig. 5.3 shows that the maximum power point increases along with the increase of the solar irradiation level. This proves one of the physical characteristics of solar array.

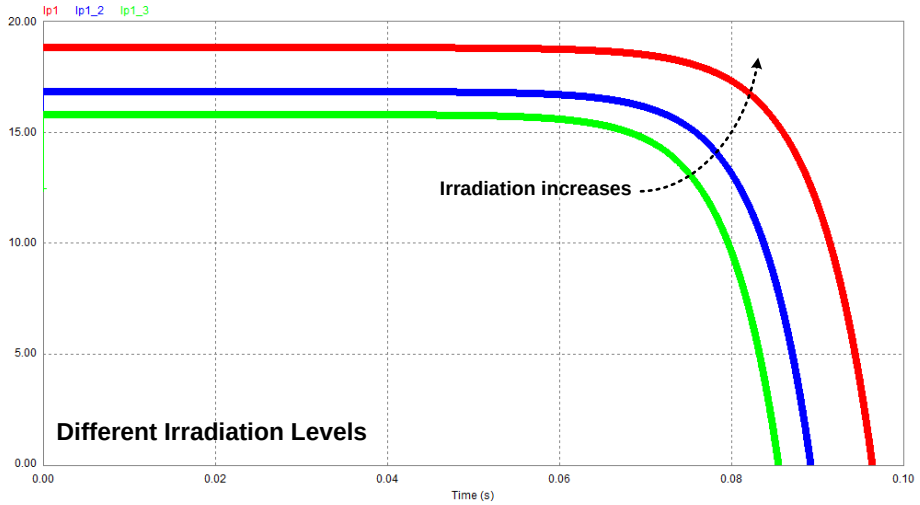

Fig. 5.2 PV current vs. PV voltage with different irradiation levels.

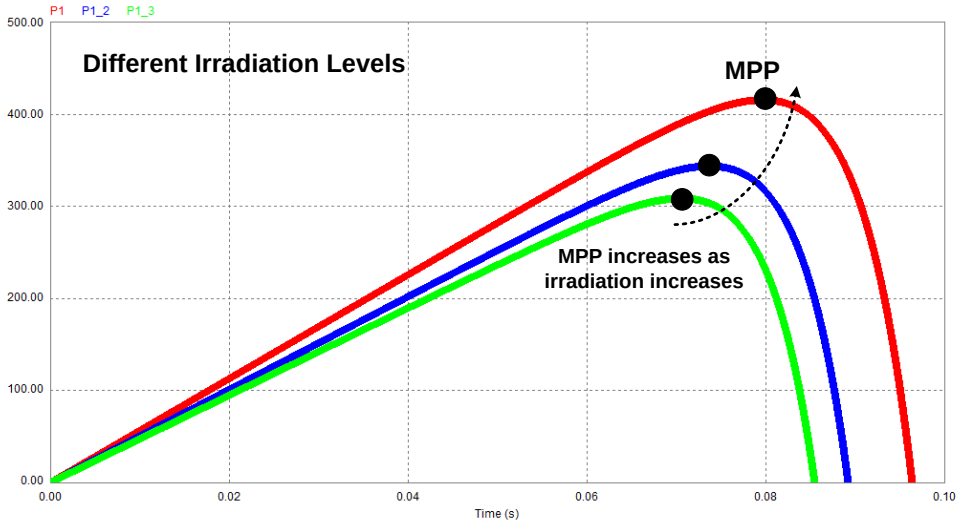

Fig. 5.3 PV power vs. PV voltage with different irradiation levels.

Temperature is another dominant factor that greatly affects the behavior of the solar array. Fig. 5.4 provides the PSIM schematic for simulating the PV characteristic curves under different temperature conditions. Similarly, the function block *m* here is provided by Eq. (5.2) as well.

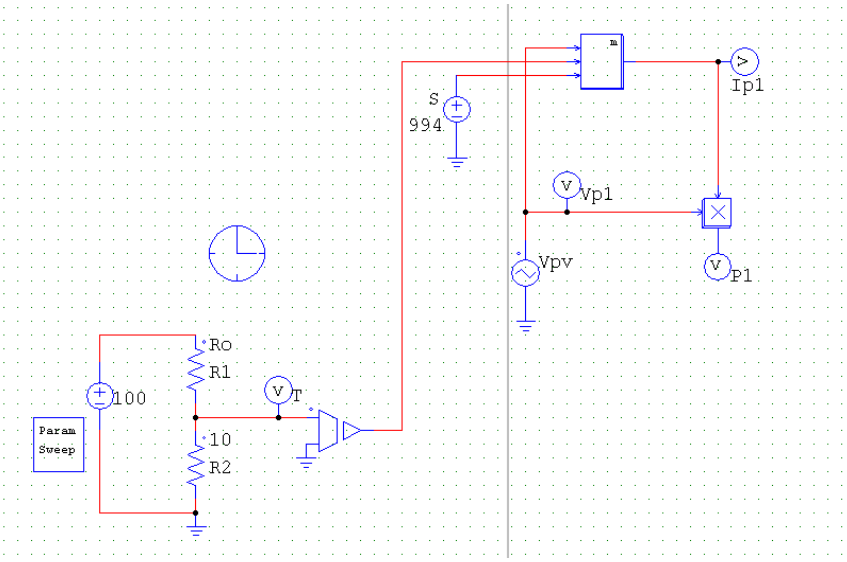

Fig. 5.4 PSIM schematic of PV array with different temperatures.

The following figures, Fig. 5.5 and Fig. 5.6, show the simulation results of the characteristic curves with respect to different environment temperatures. The results confirm that, as expected, the maximum power point is inverse proportional to the temperature. That is to say, the maximum power point decreases as the temperature increases, as shown in Fig. 5.6.

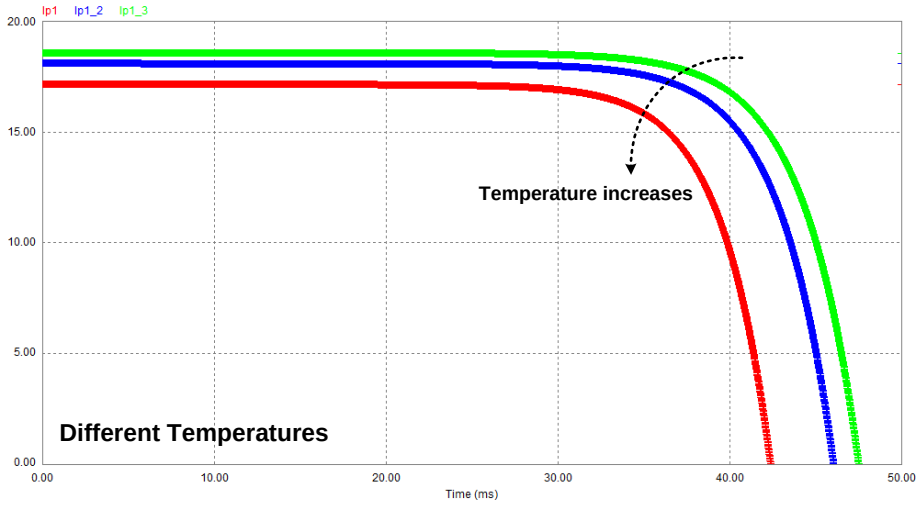

Fig. 5.5 PV current vs. PV voltage with different temperatures.

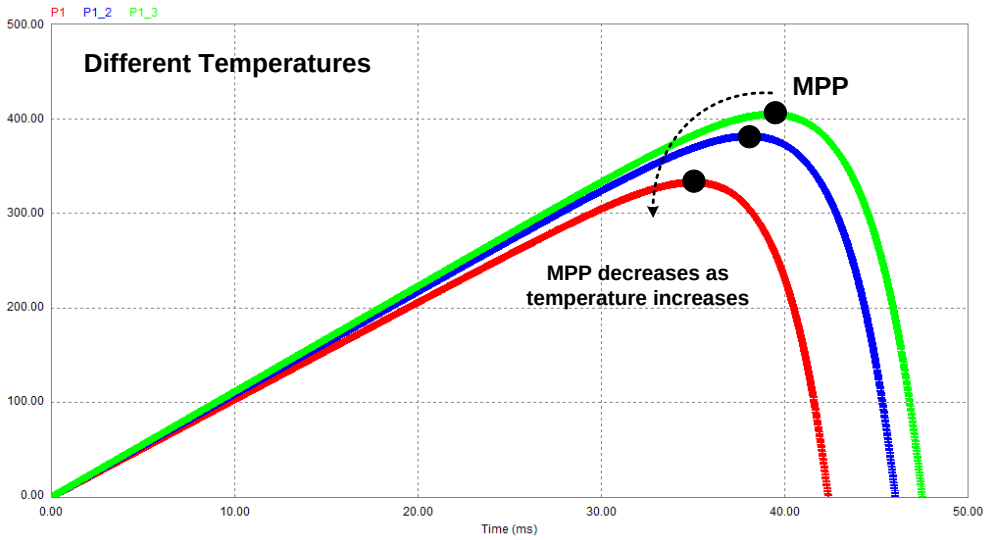

Fig. 5.6 PV power vs. PV voltage with different temperatures.

Series- and parallel- connected solar arrays act basically like a battery or a large capacitor. For the convenience of the system simulation, a large capacitor is connected to the output node of the solar array simulator as an energy storage element. Fig. 5.7 shows the solar array simulator in PSIM.

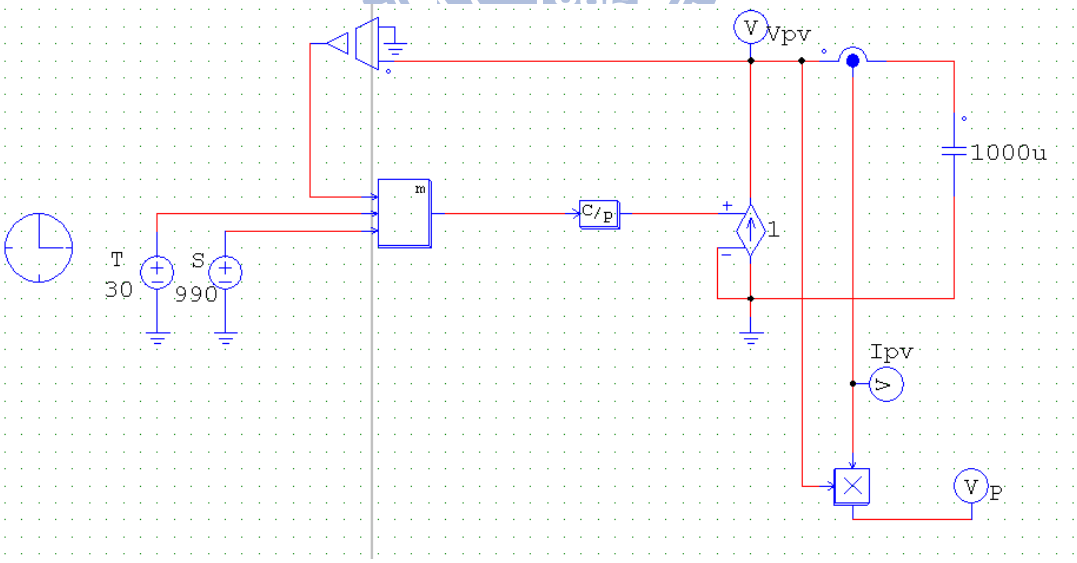

Fig. 5.7 PSIM schematic for the solar array simulator.

Fig. 5.8 demonstrates the simulated behavior of solar array at temperature of 30°C and irradiance of 990 Watt/m^2.

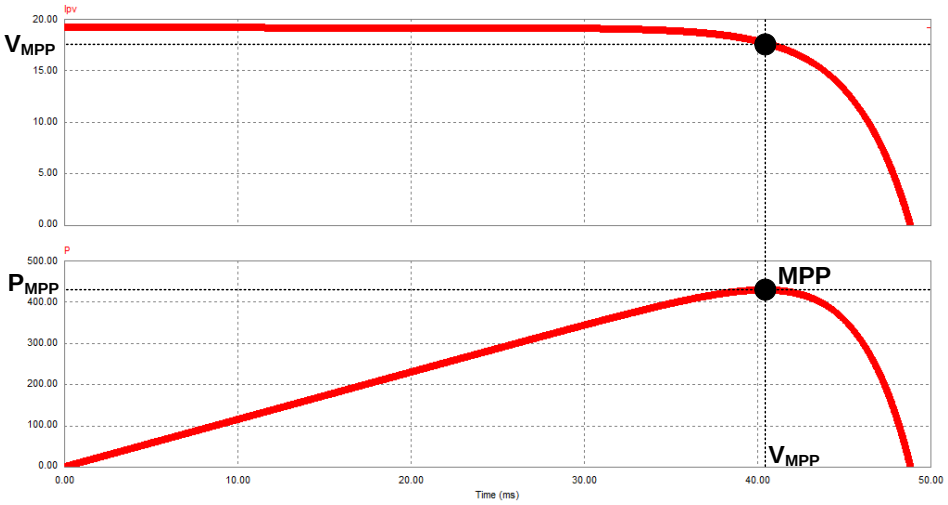

Fig. 5.8 PSIM simulated PV characteristic curves.

Fig. 5.9 shows the whole picture of the proposed maximum power point tracking technique in PSIM schematic. It can be roughly divided into four parts, as shown in Fig. 5.10 ~ Fig. 5.13.

The first part, Fig. 5.10, includes a solar array simulator and a boost converter. The solar array simulator is to provide the input current and voltage with the characteristics similar to a real solar array. The boost converter, in addition, is used to modulate the operating point and track the maximum power point.

The second part is about the slope detection tracking (SDT) circuit, as shown in Fig. 5.11. Sample-and-hold circuits here are used to sense the PV voltage and PV current information. Old voltage and current data are also stored for the use of slope calculation. In addition, arithmetic circuits, such as adder, subtractor, multiplier, are used to calculate the slope. The output of this circuit is an analog signal which indicates the value of the slope at that time instant.

The third part, shown in Fig. 5.12, is the circuit to determine the

perturbation direction. The sensed slope information serves as an input for this circuit. Then it will be compared to the value ε according to the condition given in TABLE 5.1 to determine the new reference voltage for the boost converter so as the next move of the operating point. If the slope is positive and larger than the value ε, the next move of operating point will be in a positive direction. If the slope falls in the range between ε and $-\varepsilon$, the next reference voltage will remain the same. This means that the system is already operating on or near the maximum power point. However, if the slope is smaller than $-\varepsilon$, it means the system needs to decreases the operating voltage to catch up the maximum power point. As a result, the operation will move in a negative direction. Fig. 5.13 shows the last part of the MPPT circuit which deals with the open-circuit detection (OCT) tracking. As mentioned before, OCT helps the system to locate the approximate maximum power point at the beginning. This circuit is only active during the system startup period. After the startup period, the SDT technique takes over the tracking control to track the maximum power point.

TABLE 5.1 Slope Condition vs. Perturbation Direction

Slope Condition	**Perturbation Direction**
$Slope > \varepsilon$	$V_{ref}' = V_{ref} + \Delta V$
$-\varepsilon < Slope < \varepsilon$	$V_{ref}' = V_{ref}$
$Slope < -\varepsilon$	$V_{ref}' = V_{ref} - \Delta V$

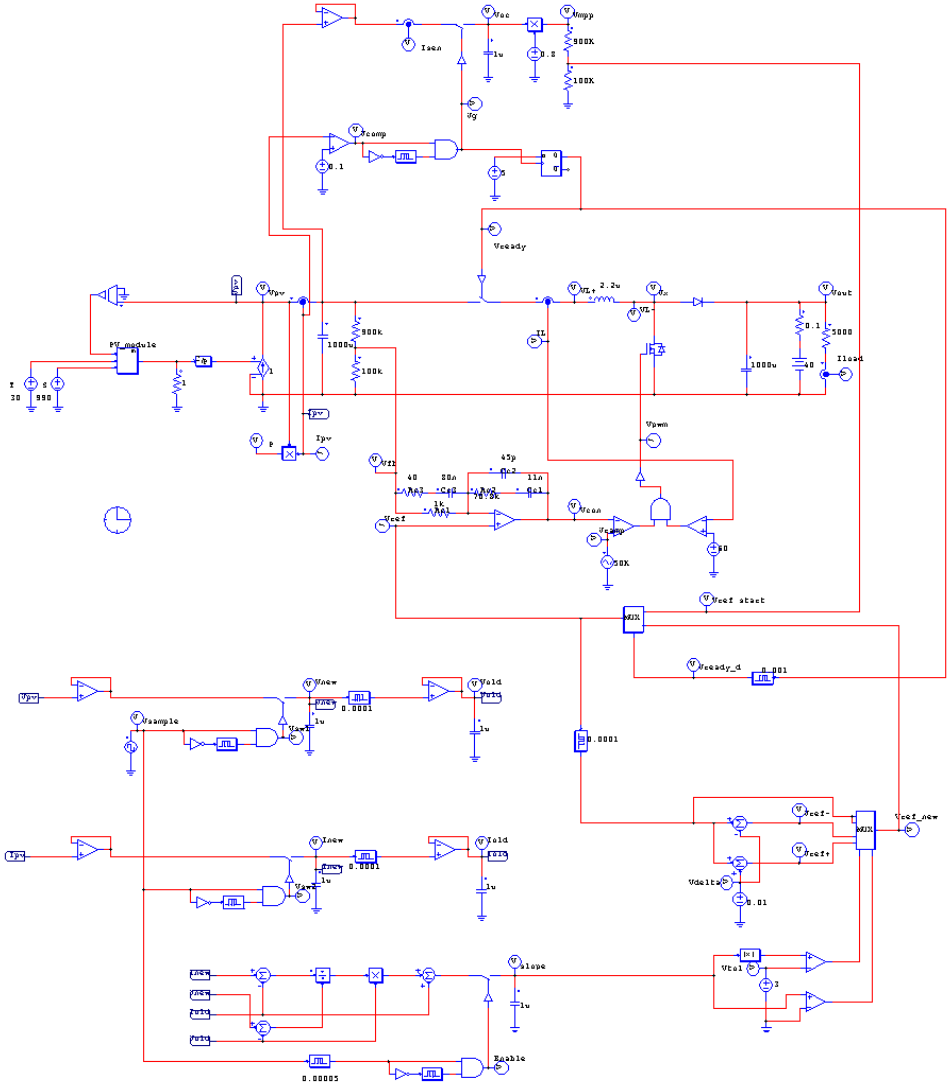

Fig. 5.9 PSIM schematic of the proposed maximum power point tracker.

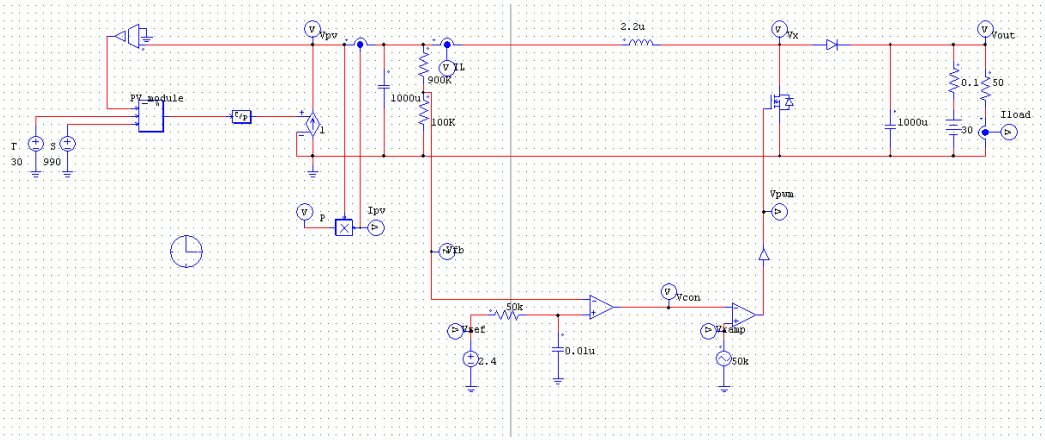

Fig. 5.10 Solar array simulator along with boost converter.

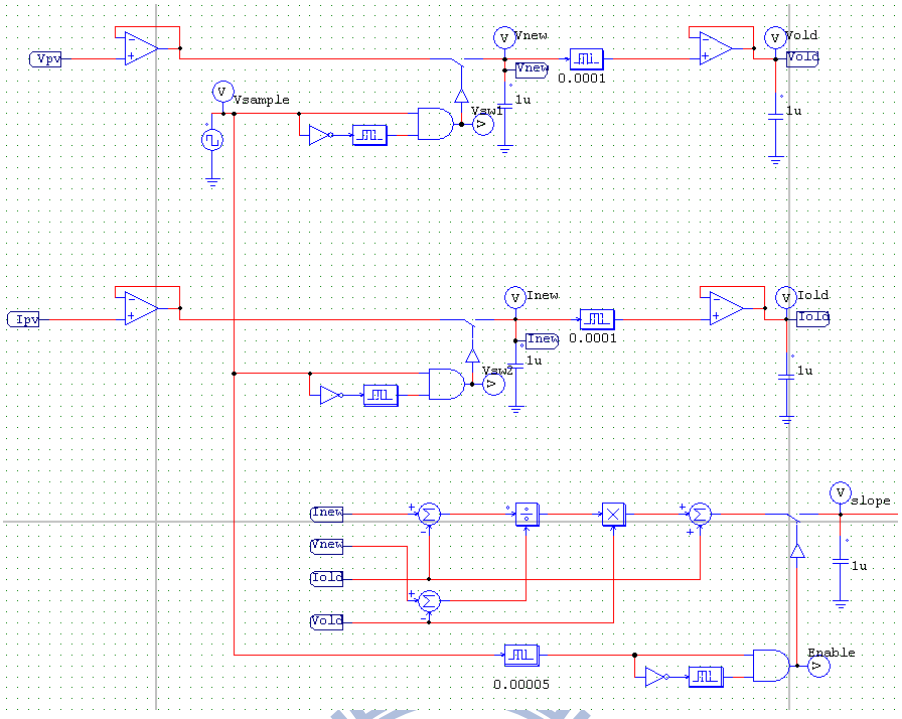

Fig. 5.11 PSIM schematic of the slope detection circuit.

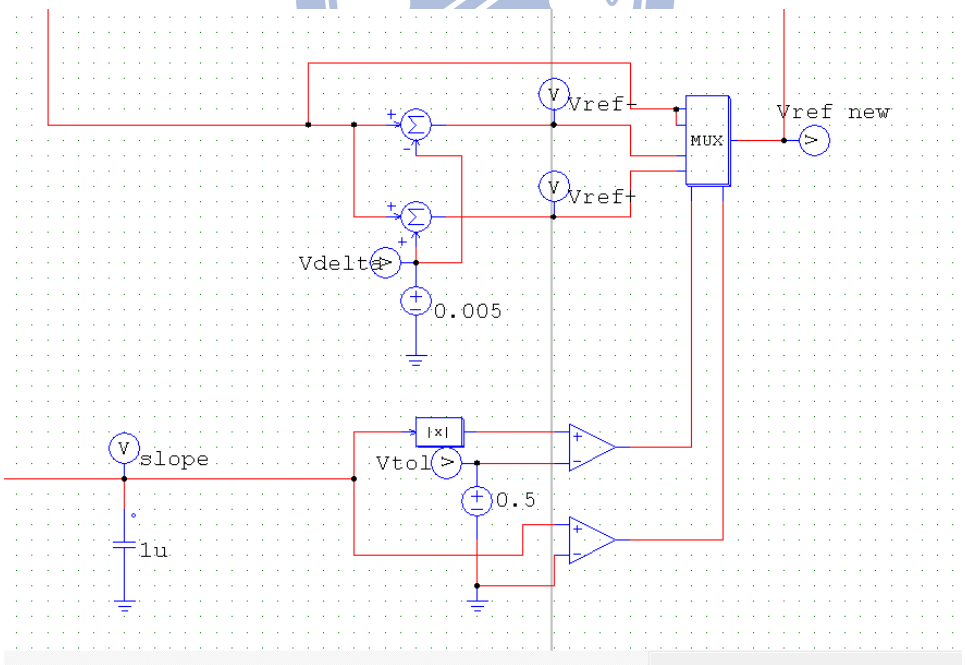

Fig. 5.12 PSIM schematic of the perturbation circuit.

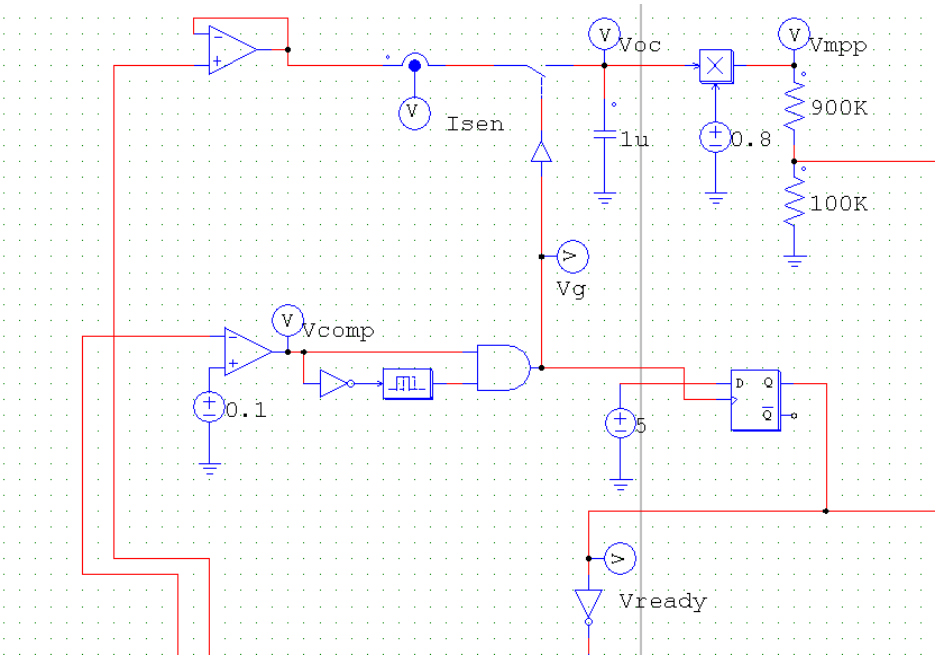

Fig. 5.13 PSIM schematic of OCT circuit.

To verify the tracking efficiency of the proposed MPPT technique, the maximum power point voltage, current, and power of the solar array simulator at a given temperature and irradiation is first investigated and then compared to the measured result. Fig. 5.14 shows the simulated solar array output information. It shows that the output voltage at the maximum power point is around 24V at the temperature of 30°C and the irradiance of 990 Watt/m^2. This means that under these environmental conditions the solar array can output its maximum power when the operating point is controlled around 24V. That is to say, the PV system needs to regulate the operating voltage around 24V to achieve a high tracking efficiency and high power conversion efficiency.

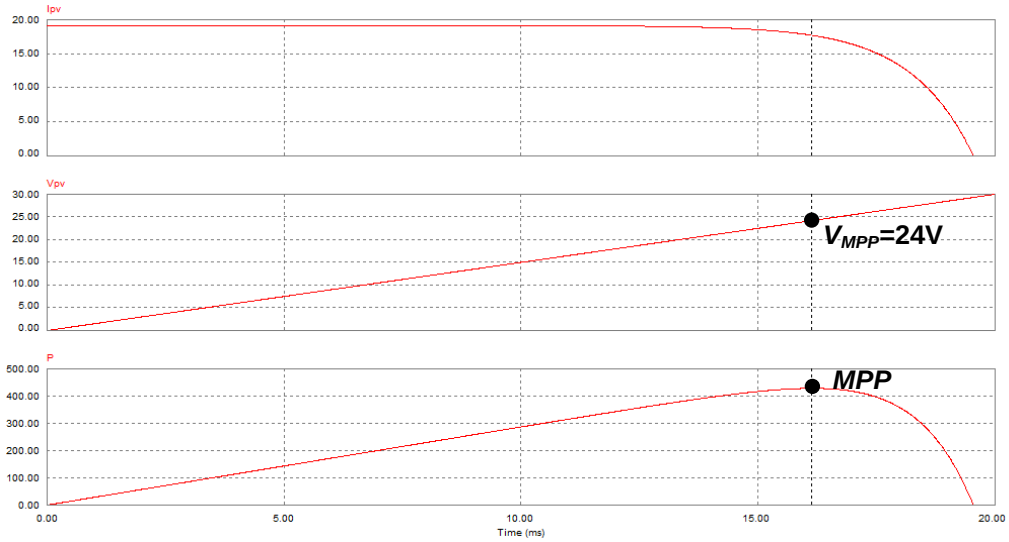

Fig. 5.14 The output of solar array simulator at 30°C and 990 Watt/m^2.

Fig. 5.15 shows the simulation waveforms of the proposed MPPT technique at the temperature of 30°C and the irradiance of 990 Watt/m^2. The tracking procedure at first undergoes the OCT period. As mentioned before, during this period, the operating point voltage is set to be around the maximum power point, approximate 70% of the open-circuit voltage. This increases the tracking speed during the system power-on period. After the OCT period, the SDT takes place the tracking control. SDT constantly detects the slope condition and changes the perturbation direction according to the polarity of the operating voltage to the maximum power point voltage. As the waveform indicated in Fig. 5.15, the settled PV voltage is around 24V, which agrees to the maximum power point voltage simulated by the solar array simulator in Fig. 5.14. This result concludes that the proposed system can effectively track the maximum power point as expected.

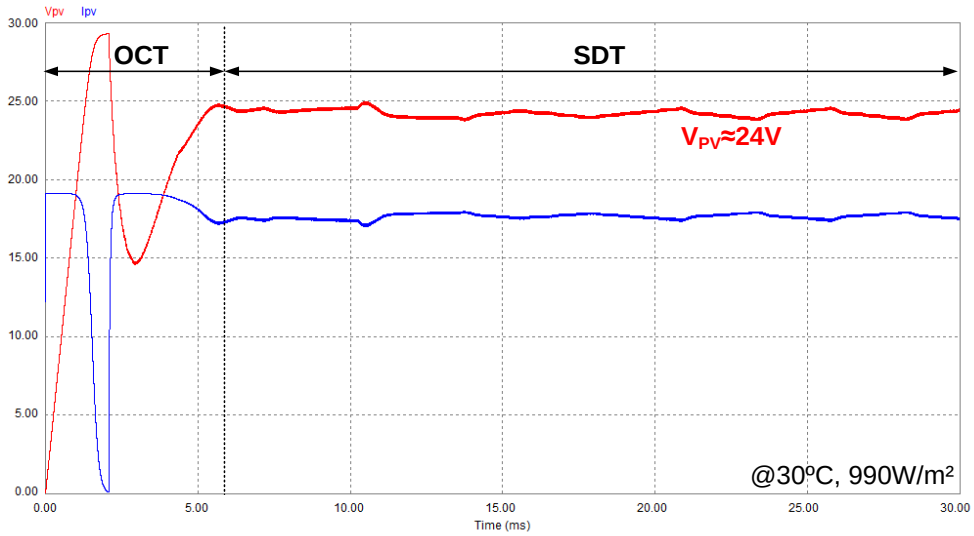

Fig. 5.15 The MPP tracking waveforms at 30°C and 990 Watt/m^2.

The solar irradiation is changed to 110 Watt/m^2 to test the tracking efficiency under low irradiation level. The simulation in Fig. 5.16 shows that the maximum power voltage is regulated around 18V and this matches the maximum power point voltage given in a solar array simulator.

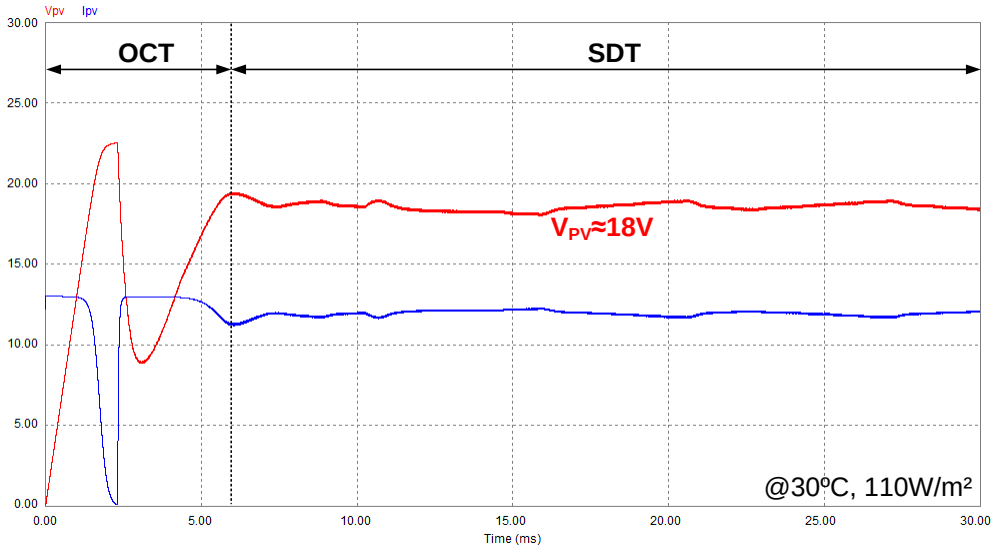

Fig. 5.16 The MPP tracking waveforms at 30°C and 110 Watt/m^2.

The solar irradiation changes periodically during the day, a good MPP

tracker needs to maintain a high performance, either fast tracking speed or high tracking accuracy, no matter the irradiation changes. The proposed tracking technique is put into an irradiation transition test in Fig. 5.17. The solar radiation changes from 990 Watt/m^2 to 110 Watt/m^2. As can be seen in the figure, the PV voltage successfully changes from 24V to 18V. This guarantees the universality of the proposed maximum power point tracking technique.

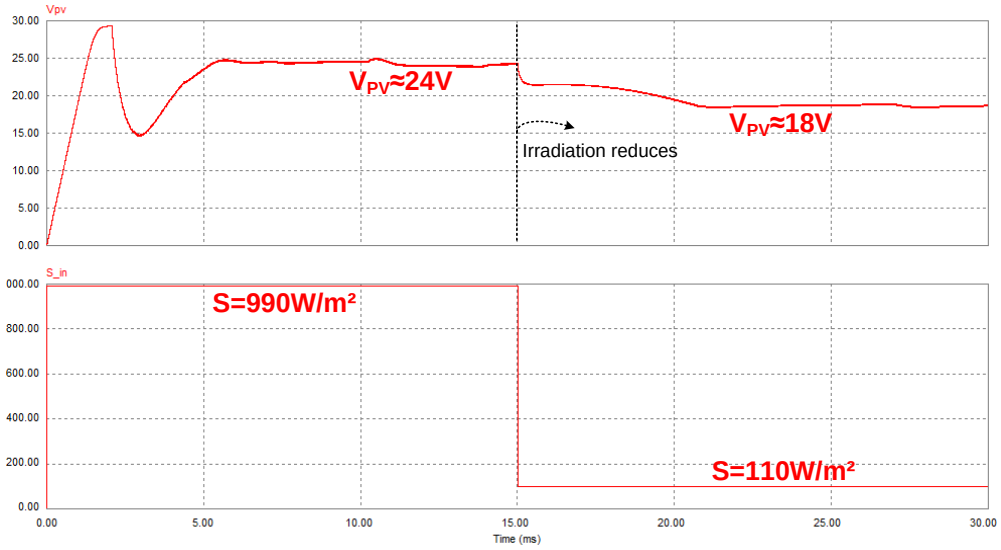

Fig. 5.17 The PSIM simulation waveforms under irradiation transition.

A versatile PV system needs to handle a wide temperature range as well, not only in a high temperature environment but also in a low temperature. Here both high temperature 50°C and low temperature 5°C are put into test, as shown in Fig. 18 and Fig. 19, respectively. The tracking undergoes the same tracking procedure as in previous examples. First is the OCT and then the SDT takes place. In either temperature, the high tracking efficiencies are both guaranteed. At high temperature 50°C, the PV voltage is controlled around 23.5V. And at low temperature 5°C, the PV

voltage settles at around 25V. The solar irradiation in both cases is controlled as 990 Watt/m^2.

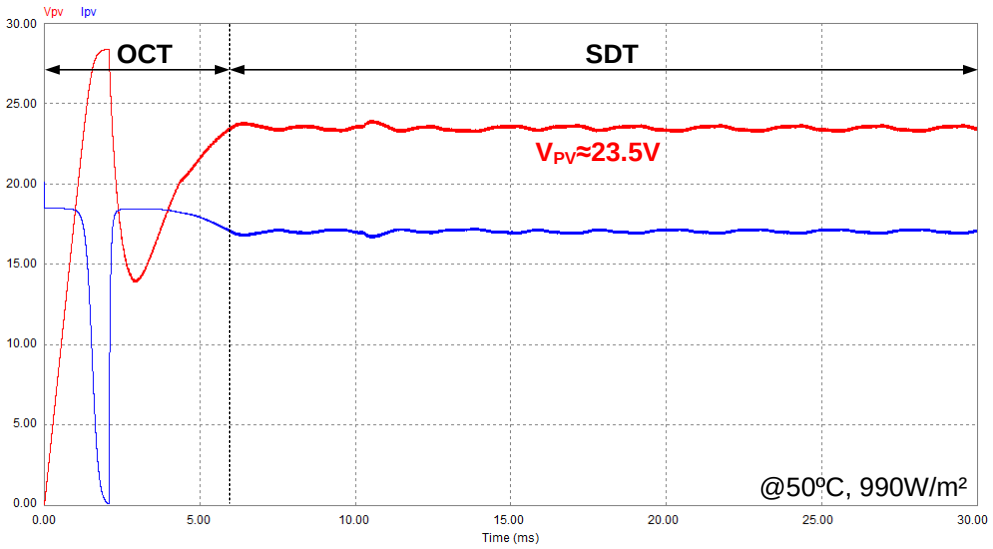

Fig. 5.18 The MPP tracking waveforms at 50°C and 990 Watt/m^2.

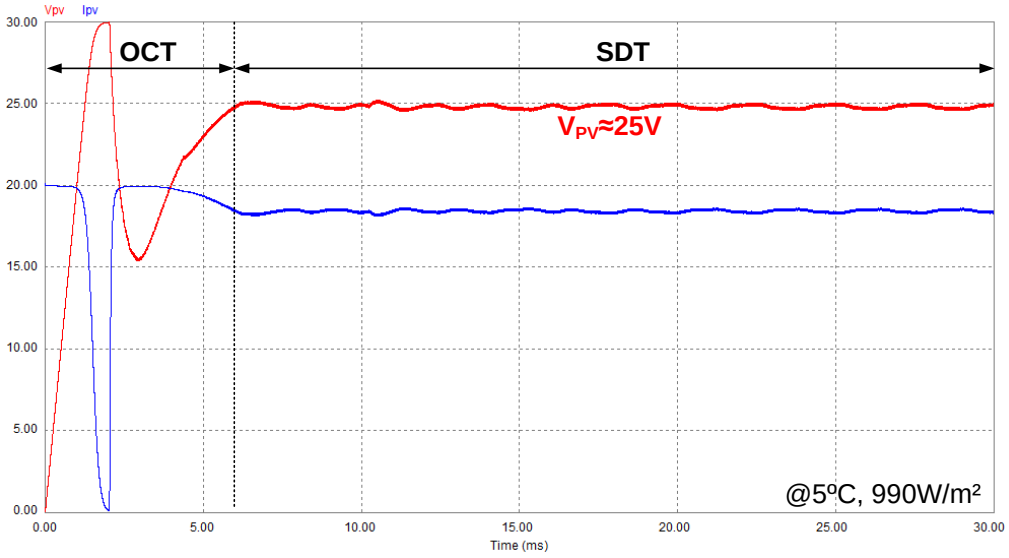

Fig. 5.19 The MPP tracking waveforms at 5°C and 990 Watt/m^2.

The tracking performance during the temperature transition is examined in Fig. 5.20. As the temperature changes from high temperature of 50°C to low temperature of 5°C, the PV voltage changes from 23.5V to 25V with little time delay. The waveforms confirm the effectiveness of the

proposed tracking technique and the circuit under the drastic temperature changes.

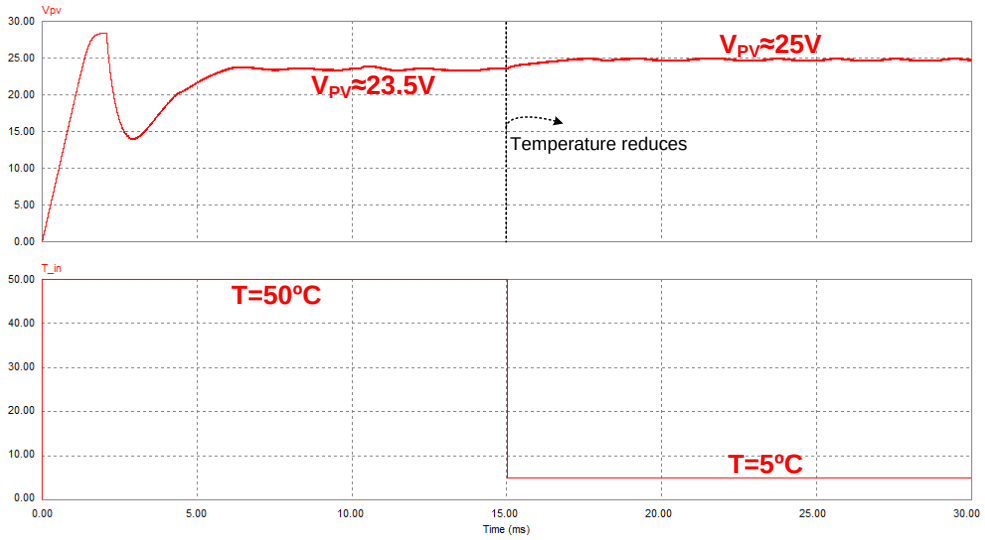

Fig. 5.20 The PSIM simulation waveforms under temperature transition.

The PSIM simulations discussed in this section help confirm the effectiveness of the proposed maximum power point tracking algorithm and the robustness of the maximum power point tracking circuits. The simulation results show that the proposed maximum power point tracker can not only track the maximum power point accurately under varying solar irradiation but also work perfectly under the drastic temperature changes.

5.1.2 HSPICE Simulations

The PSIM simulations mentioned in last section confirmed the effectiveness of the proposed MPPT algorithm. In this section, the HSPICE simulations are introduced to assist the circuit level design.

Based on the equivalent circuit of PV module shown in Fig. 2.1and referred to the parameters provided during the PSIM simulation, Fig. 5.21 shows the HSPICE simulation of the solar array. The short-circuit current, I_{SC}, and the open-circuit voltage, V_{OC}, are proportionally downgraded to a reasonable range, which are 50μA and 1.5V, respectively. This equivalent circuit, or the solar array simulator, behaves similarly like a real solar array. The solar array current, I_{PV}, increases inverse proportionally to the increment of the solar array voltage, V_{PV}. And there exists a maximum power point where the solar array outputs its maximum energy.

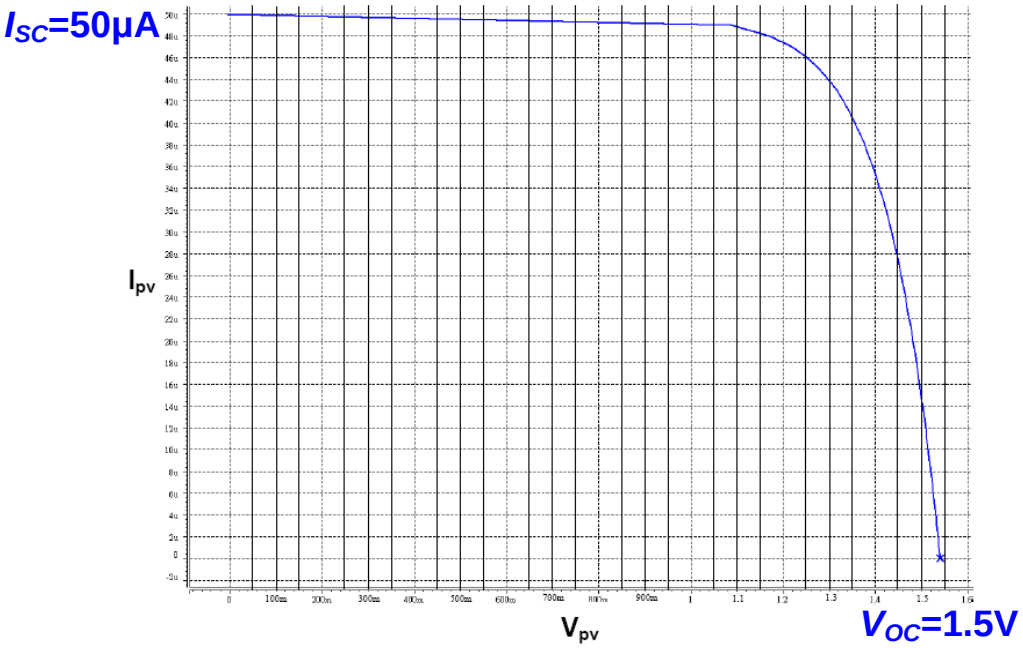

Fig. 5.21 The HPSICE I-V simulation of the solar array.

The environment factors, which are temperature and solar irradiation, basically change the parameters in the solar array to affect its performance, e.g. the maximum power point. Theses parameters include the parasitic series resistor, R_S, the parasitic parallel resistor R_P, the diode saturation current, I_S, and the diode quality factor, n. Fig. 5.22 demonstrates the influences of these

parameters on the MPP while others are fixed. Fig. 5.22(a) shows that the MPP increases along with the increase of R_S, while the MPP increment is small. In Fig. 5.22(b), it shows that the MPP changes proportionally to R_P. The increments, however, are barely noticeable. The influences of I_S on the MPP are depicted in Fig. 5.23(c). Obviously, the MPP decreases as I_S increases, which means they are inverse proportional to each other. Furthermore, Fig. 5.24(d) shows the relationship between the MPP and n. It is apparent that the MPP increases dramatically when n increases.

In summary, all of these four parameters, R_S, R_P, I_S, and n, have their effects of the MPP, either proportionally or inverse proportionally. Among all of these parameters, n has the most significant influence on the MPP. As a result, it is chosen as the varying parameter to emulate the changes in the atmosphere, so to say, the environment temperatures and the solar irradiation levels. TABLE 5.2 lists the simulated results of V_{OC} and V_{MPP} depending of different diode quality factors. With the help of the information given in TABLE 5.2, one can use different n values to simulation different MPPs. The target of the MPPT circuit is to track the MPPs as close as possible to these simulated MPPs.

TABLE 5.2 Diode Factor vs. Maximum Power Point Voltage

Diode Factor (n)	**Open-Circuit Voltage (V_{OC})**	**Maximum Power Point Voltage (V_{MPP})**
12	4.62V	3.56V
11	4.23V	3.25V
10	3.84V	2.91V
9	3.45V	2.60V
8	3.06V	2.28V

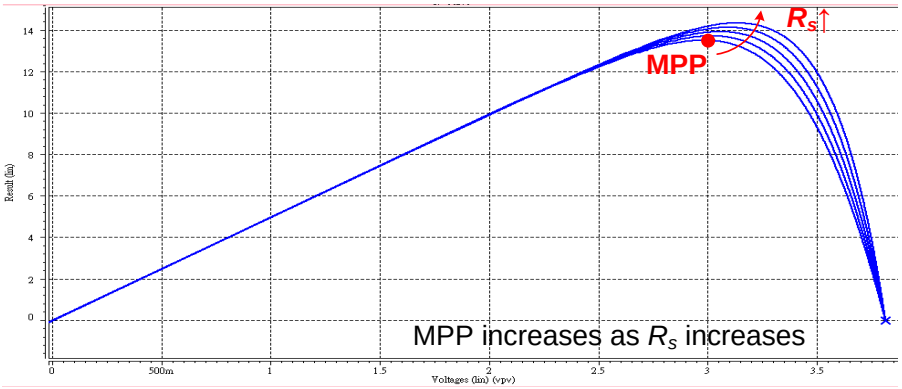

(a)

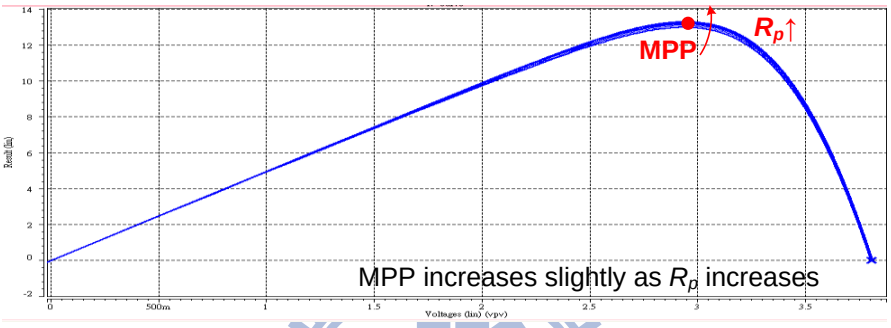

(b)

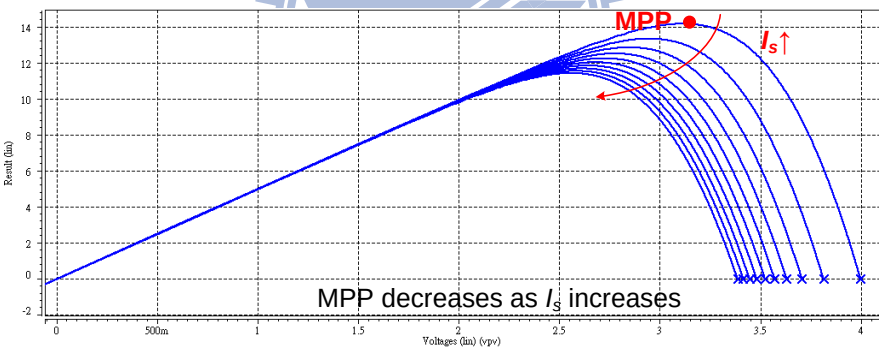

(c)

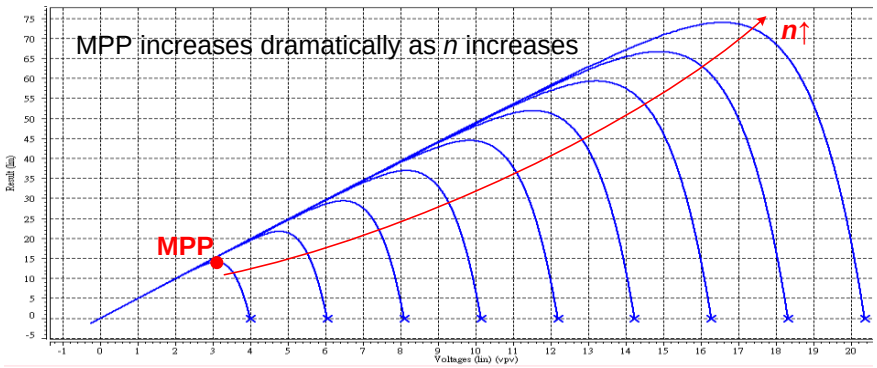

(d)

Fig. 5.22 The simulated characteristic P-V curves according to different parameters. (a)Varying R_S. (b) Varying R_P. (c) Varying I_S. (d) Varying n.

As mentioned in Chapter 4, the 7-bit up/down counter modulates the duty cycle of the boost converter after receiving the slope information from the slope detection circuit. The current flowing out of the solar array is then adjusted accordingly to pull down or push up the operating voltage, in order to approach the MPP. Fig. 5.23 gives the simulation results of the duty cycle modulation according to the slope changes from positive to negative and from negative to positive.

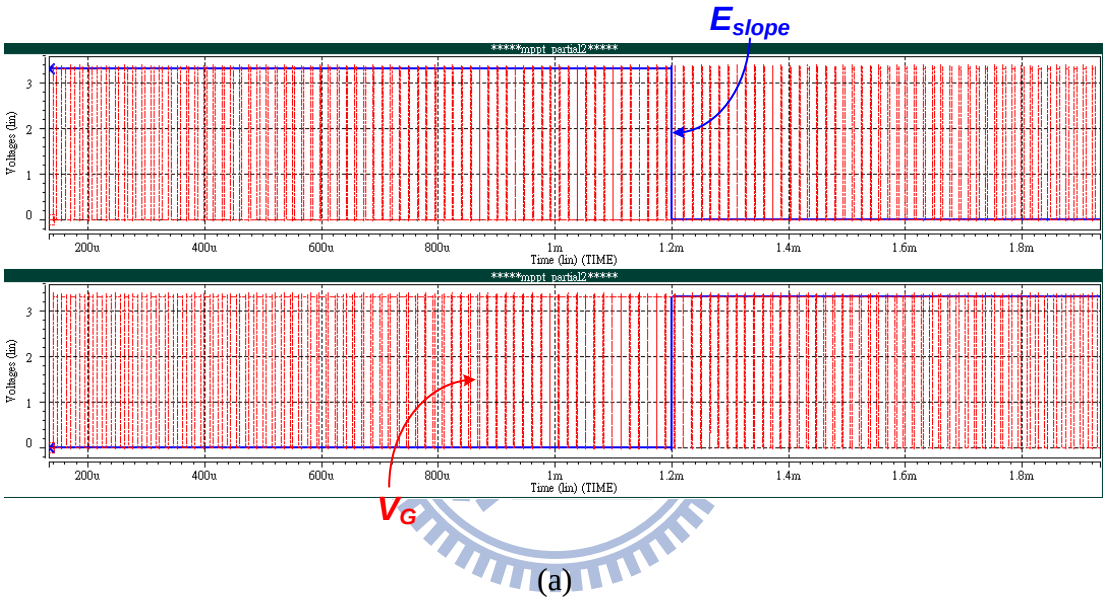

(a)

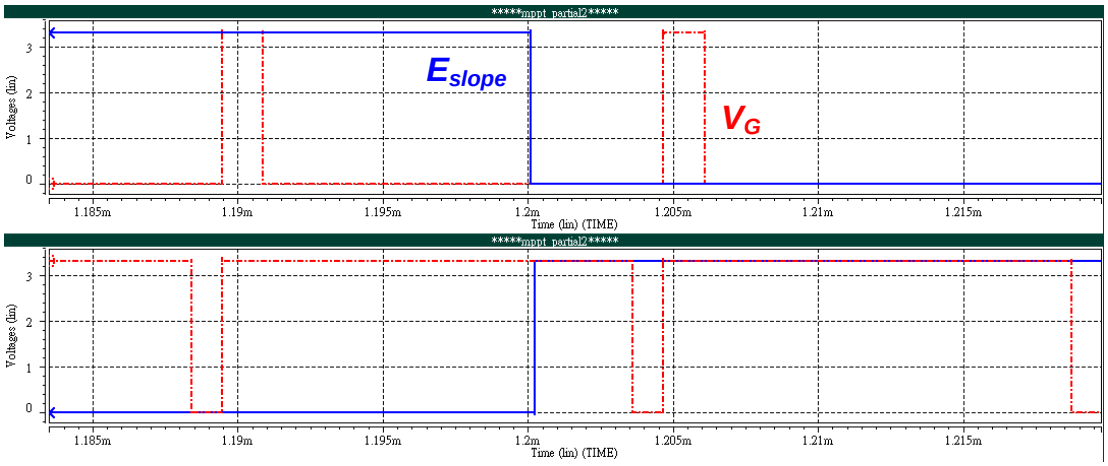

(b)

Fig. 5.23 Simulation waveforms of duty cycle modulation. (a) The changes in V_G according to the changes in slope polarity. (b) The zoom-in view of (a).

Fig. 5.24(a) shows the case when the slope changes from positive to negative or E_{slope} changes from high to low. Fig. 5.24(b) depicts the initial waveforms before the duty cycle modulation occurs. The slope condition E_{slope} is detected as high in Fig. 5.24(c), which means the operating point falls on the left-hand side plane on the power-voltage curve. This results in the decrement of the duty cycle to reduce the current of solar array. The operating voltage, as a consequence, is pulled up to approach the MPP. When the slope condition E_{slope} is found to be low, it means the operating point falls on the right-hand side of the power-voltage plane. Under this condition, the duty cycle is then increased to pull more current from the solar array. The operating voltage is again reduced to pursue the MPP, as shown in Fig. 5.24(d).

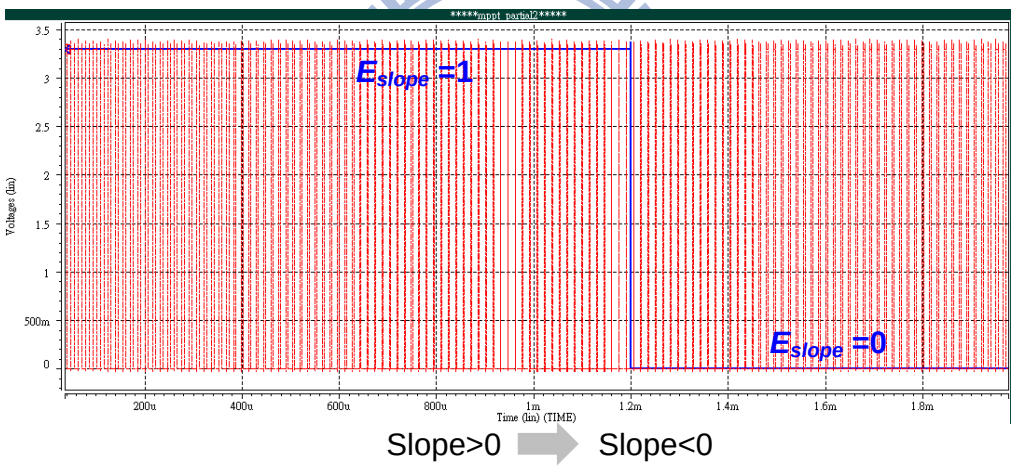

(a)

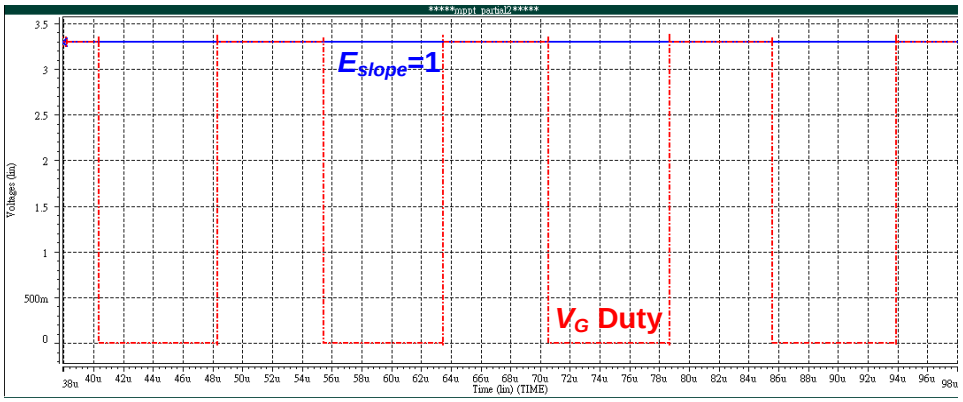

(b)

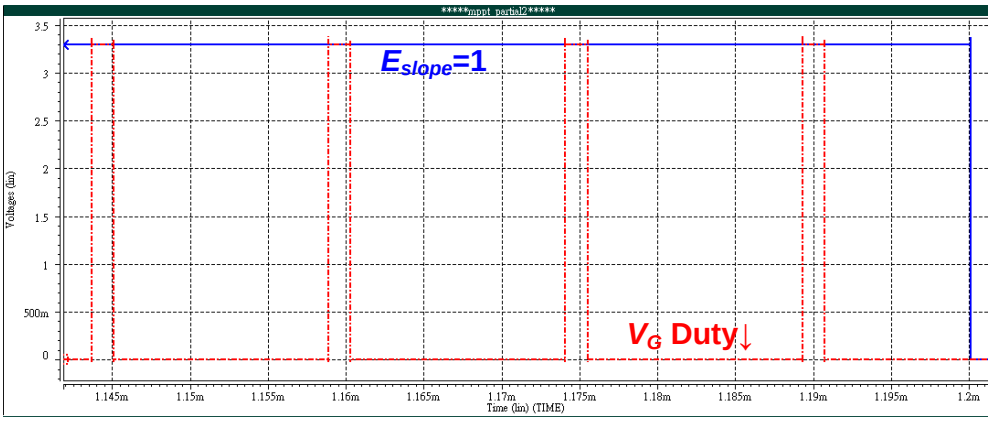

(c)

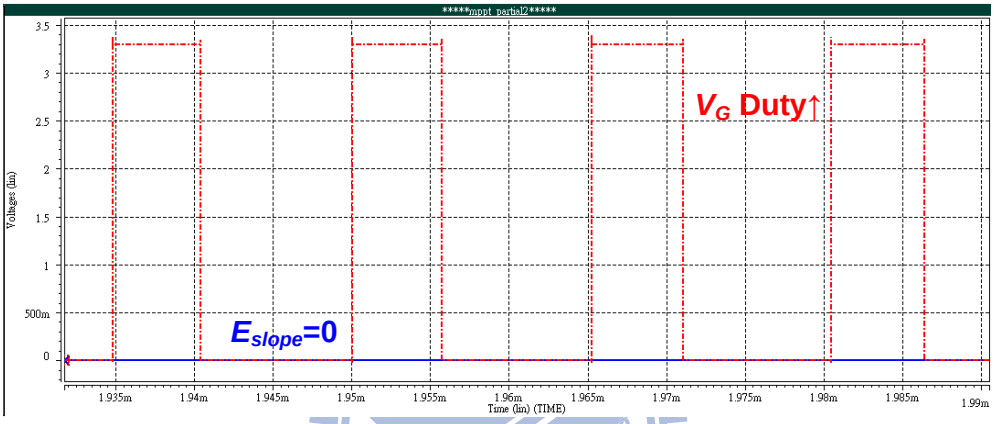

(d)

Fig. 5.24 Duty cycle changes when the slope changes from positive to negative. (a) The waveforms of E_{slope} vs. V_G. (b) Initial duty cycle. (c) When E_{slope} is detected as high. (d) When E_{slope} is detected as low.

On the other hand, as the slope changes from negative to positive, the duty cycle changes as shown in Fig. 5.25(a). Fig. 5.25(b) shows the initial waveforms before the slope changes. When the slope is detected to be negative, the duty cycle increases to increase the solar array current and therefore decrease the voltage to track the MPP as can be seen in Fig. 5.25(c). On the other hand, the slope is positive after the slope transition, which means the operating point falls on the left-hand side of the power-voltage plane. The duty cycle, consequently, needs to decrease in order to raise the solar array voltage as shown in Fig. 5.25(d).

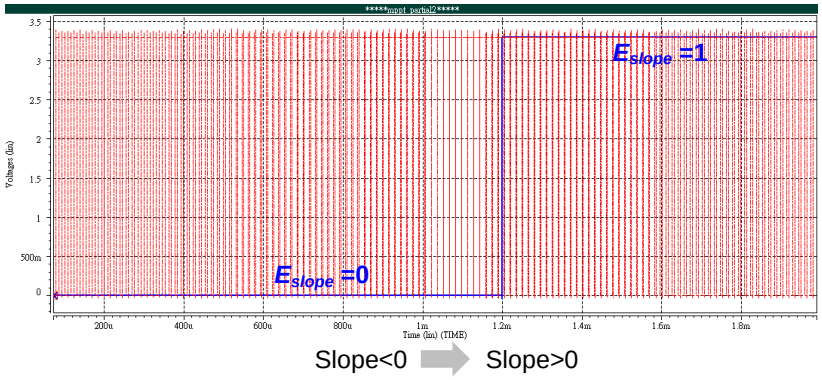

(a)

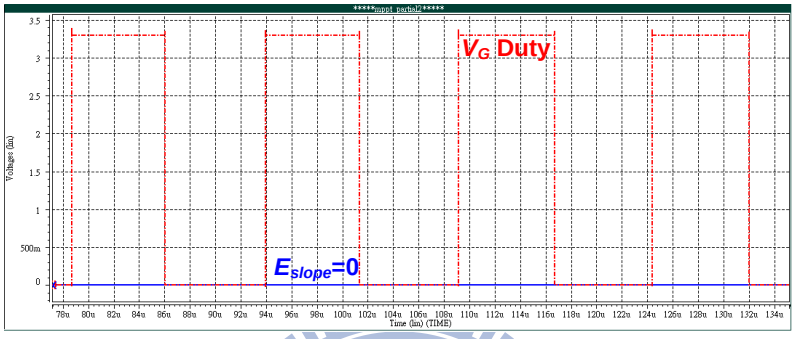

(b)

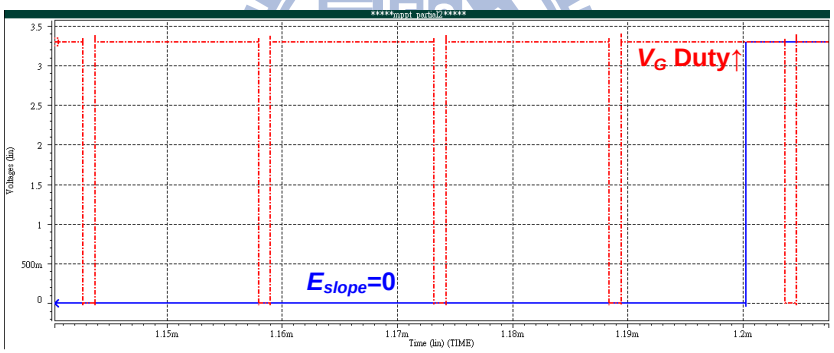

(c)

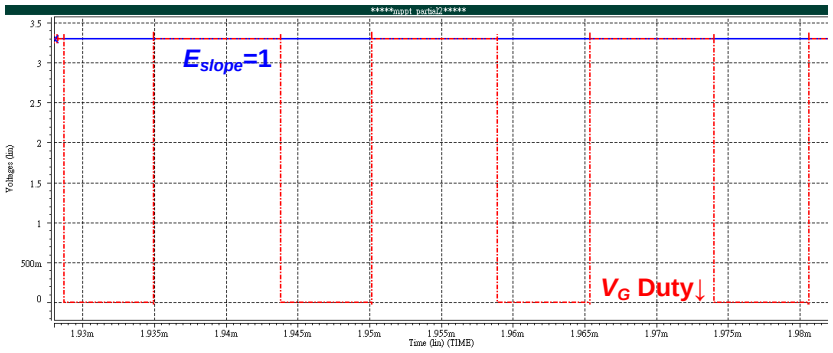

(d)

Fig. 5.25 Duty cycle changes when the slope changes from negative to positive. (a) The waveforms of E_{slope} vs. V_G. (b) Initial duty cycle. (c) When E_{slope} is detected as low. (d) When E_{slope} is detected as high.

Fig. 5.26 shows the simulation results, both the solar array voltage V_{PV} and current I_{PV}, of the proposed MPPT algorithm and circuit. Comparing the simulation results (V_{MPP}) with respect to different diode quality factors n given in TABLE 5.2, it concludes that the proposed MPPT technique can track the maximum power point of solar array and achieve a high tracking efficiency. The simulation results show that the tracking begins with the proposed OCT technique, which detects the open-circuit voltage of the solar array and approximates the operating voltage to around 70% of the open-circuit voltage. The proposed SDT technique then takes place the tracking procedure to accurately track the MPP. Owing to the oscillation around the MPP, both the voltage and current waveforms present certain oscillations during the steady-state, as can be seen in the figure.

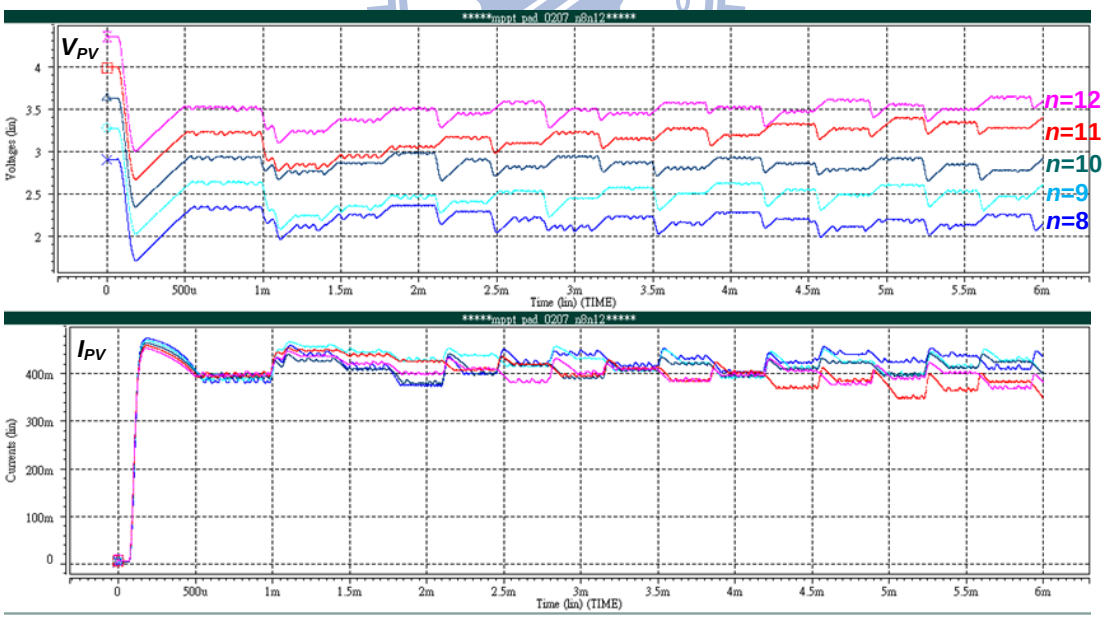

Fig. 5.26 Simulation results of the proposed MPPT technique.

As mentioned before, the proposed OCT technique is aimed to improve the tracking speed during the system power-on period. To show the

effectiveness of the OCT technique, OCT is turned off deliberately in Fig. 5.27 to compare the tracking speed to the one when it is enabled. It is apparent in the figure that the OCT technique greatly improves the tracking speed during the power-on period. In both cases, whether the OCT technique is enabled or not, the steady-state voltage reaches at 2.91V when the diode quality factor is set to 10 according to TABLE 5.2.

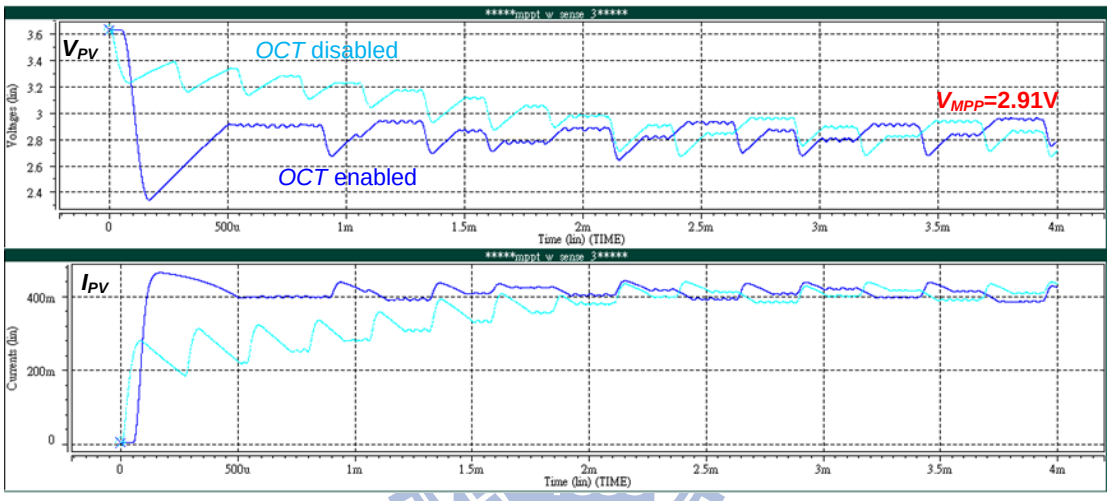

Fig. 5.27 Simulation results showing the effectiveness of the OCT technique.

To investigate the effectiveness of the proposed MPPT technique and circuit undergoing environmental condition changes, the diode quality factor *n* is changed from a high value to a low value and from a low value to a high value in Fig. 5.28(a) and Fig. 5.28(b), respectively. The diode quality factor is changed from 10 to 9 in Fig. 5.28 (a) to emulate either the increasing of irradiation level or the decreasing of ambient temperature. The simulation results, V_{MPP} transiting from high to low, confirm the speculations stated in Chapter 2. Furthermore, the tracking efficiency is high as the steady-state voltage almost coordinates to the information given in TABLE 5.2. In Fig.

5.28(b), the effectiveness of the proposed MPPT technique is examined from another perspective. The diode quality factor is changed from 9 to 10 to simulate either the decreasing of irradiation level or the increasing of ambient temperature. The simulation results show that the tracking efficiency is again guaranteed.

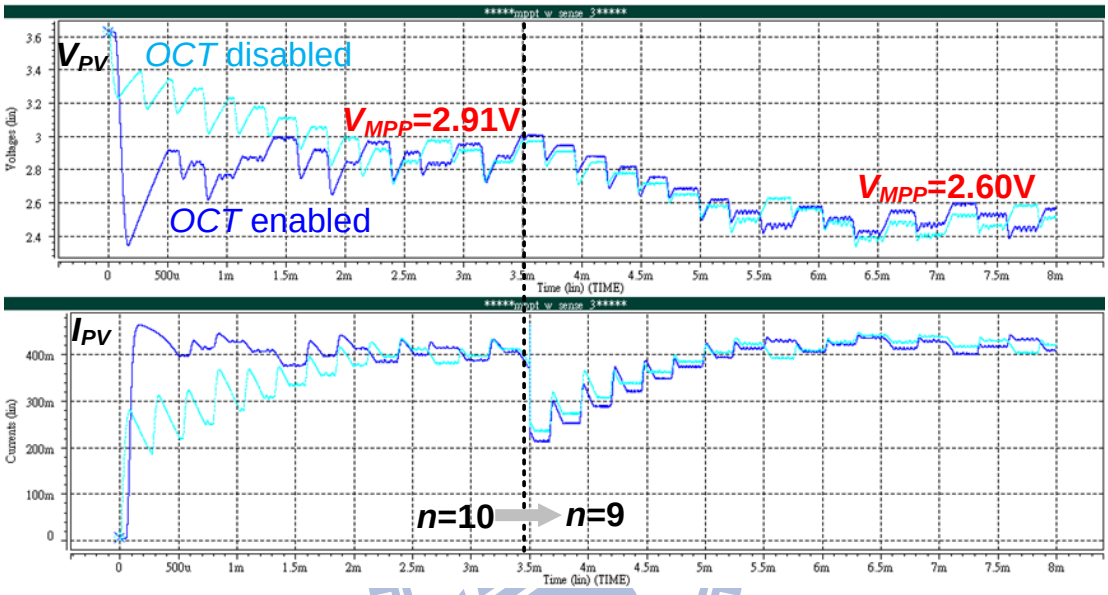

(a)

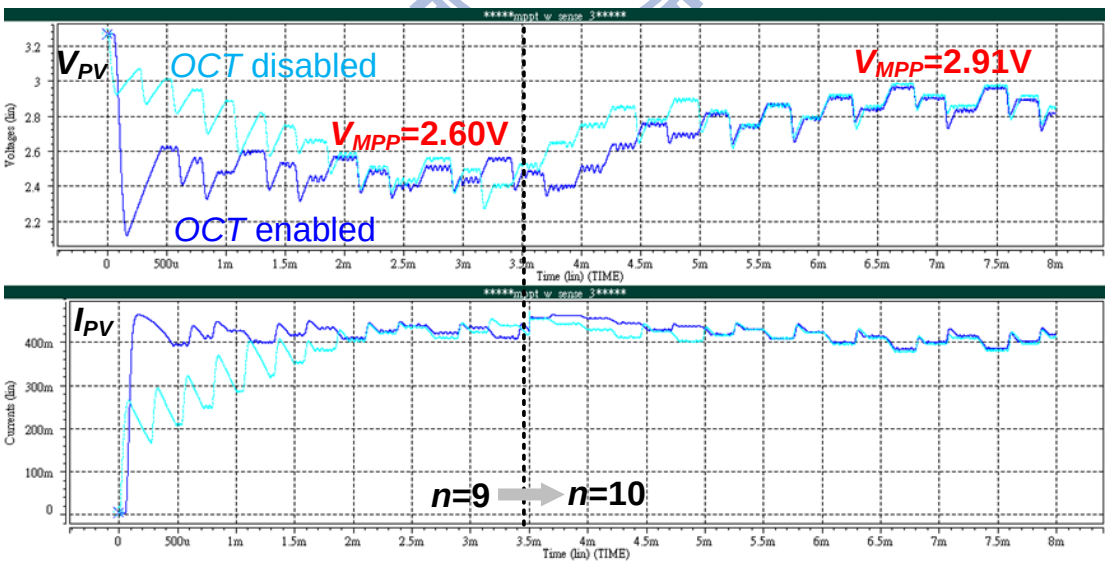

(b)

Fig. 5.28 Simulation results of the proposed MPPT technique undergoing environmental condition changes. (a)When the irradiation decreases or the temperature increases. (b)When the irradiation increases or the temperature decreases.

In conclusion, the HSPICE simulation results confirm the effectiveness of the proposed MPPT algorithm and circuit. The tracking speed during the power-on period is dramatically improved, as speculated in Chapter 3, when the proposed OCT technique is activated. High tracking accuracy, in addition, is also guaranteed since the proposed SDT technique is used.

5.2 Experiment Results

The test chip, which contains both the proposed MPPT circuit and the controller for the boost controller, was fabricated in 0.25μm BiCMOS-DMOS (BCD) 40V 1P4M process. Fig. 5.29 shows the experimental setup, the prototype and the chip micrograph of the controller for the boost converter. The solar array used in the measurement is Tynsolar TYN-285P6 [38]. TABLE 5.3 gives the technical specifications of the used solar array.

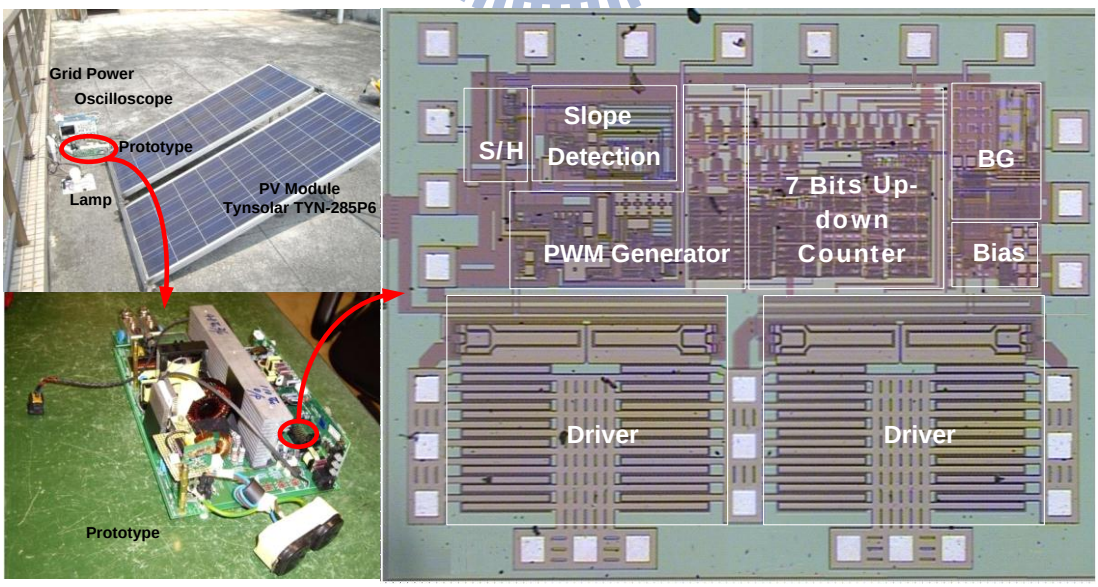

Fig. 5.29 Experiment prototype and chip micrograph.

TABLE 5.3 Technical Specifications of TYN-285P6

Maximum Power	285W
Tolerance	±5%
Open circuit Voltage	44.21 V
Short circuit Current	8.32A
Maximum Power Voltage	36.79V
Maximum Power Current	7.75A
Module Efficiency	14.61%
Solar Cell Efficiency	16.37%
Operating Temperature	-40℃ ~85℃
Short Circuit Current Temperature Coefficient	+4.500 mA/℃
Open Circuit Voltage Temperature Coefficient	-0.1500 V/℃
Maximum Power Temperature Coefficient	-0.4982 %/℃

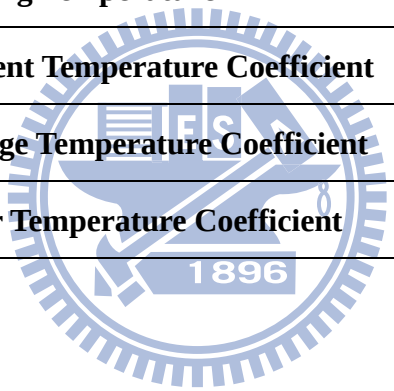

The tracking efficiency of the MPPT circuit can be approximated to the following equation [39].

$$\eta_{MPP} = \frac{P_{PV,tracked}}{P_{PV,\max}} \times 100\% \tag{5.3}$$

$P_{PV,tracked}$ is the actual energy the system captured and delivered from the solar array. $P_{PV,max}$ is the maximum energy from the sun at a specific time instant, temperature and solar irradiation. Fig. 5.30 shows the measured maximum power point tracking efficiency based on the proposed tracking algorithm and circuit.

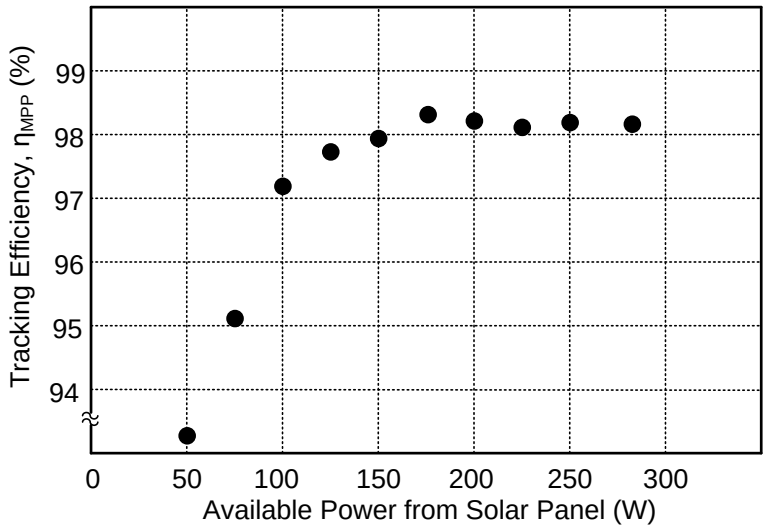

Fig. 5.30 Tracking efficiency of the proposed MPPT algorithm and circuit.

The tracking efficiency is higher than 97.3% in the available power range from 100W to 300W at ambient temperature of 28˚C. The tracking efficiency is limited below 98%, compared to contemporary product [40] due to some reasons: the process variation during the silicon fabrication, temperature variation, IC layout optimization, and the limited operation range of the calculation circuit such as the multiplier, the adder and subtractor. An overflow or underflow current may cause the circuit to misinterpret the slope condition. As a result, it undermines the tracking efficiency.

Fig. 5.31 shows the waveforms of the PV system during the power-on period. At the time the PV system turns on, the OCT technique is enabled to adjust the operating voltage close to the value of 0.7×VOC. During this open-circuit voltage detection period, the duty cycle is set to its maximum value to enhance the tracking speed. After that, the SDT technique takes over the tracking procedure to improve the tracking accuracy. When the slope detection circuit detects the slope condition is positive, which means E_{slope} is high, the duty cycle decreases, as shown in Fig. 5.31(a), to reduce the inductor

current and therefore increase the operating voltage toward the MPP. Conversely, as shown in Fig. 5.31(b), when the slope condition is detected as negative, E_{slope} is set low, the controller increases the duty cycle to the boost converter. As a result, the inductor current increases to lower the operating voltage of the system.

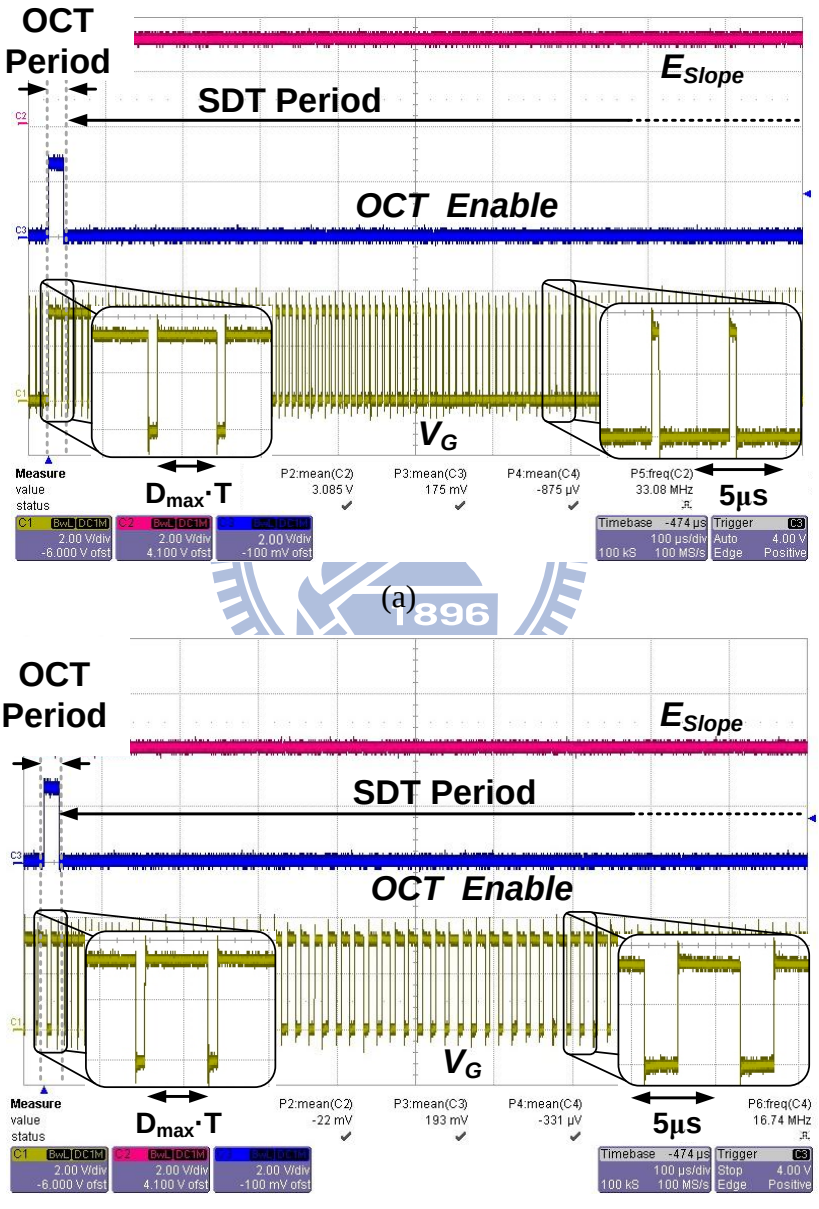

Fig. 5.31 The waveforms of PV system during the system power-on period. (a) When the detected slope condition is positive. (b) When the detected slope condition is negative.

Fig. 5.32 shows the duty cycle transitions when the solar irradiation changes. The detected slope condition changes either from negative to positive or from positive to negative depending on the solar irradiation level. In Fig. 5.32(a), when the solar irradiation level increases, the duty cycle of the control signal, V_G, which controls the gate of the power NMOS (M_N), gradually decreases to a smaller value. On the contrary, in Fig. 5.32(b), V_G changes from small duty cycle to large duty cycle when the detected slope condition transits from positive to negative, which is due to the degradation of the solar irradiation level.

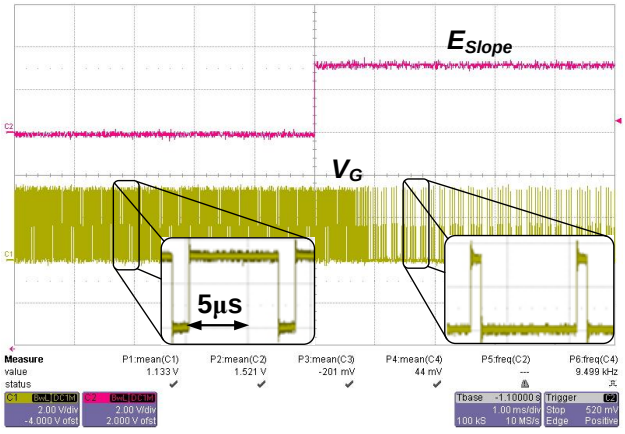

(a)

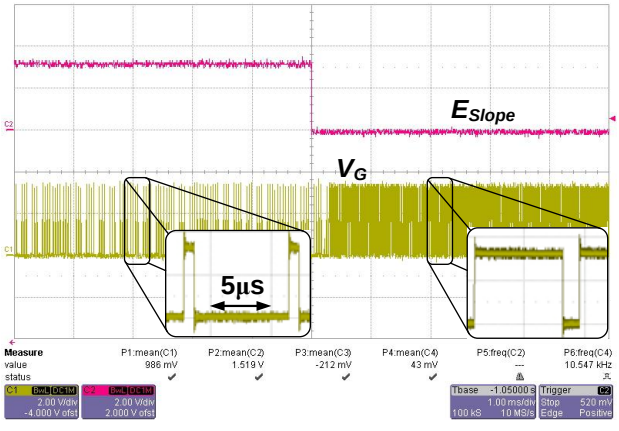

(b)

Fig. 5.32 The waveforms of V_G according to different E_{slope} values. (a) When the solar irradiation level increases, E_{slope} changes from low to high. (b) When the solar irradiation level decreases, E_{slope} changes from high to low.

Fig. 5.33 shows some waveforms to investigate the tracking speed during the system power-on period. In Fig. 5.33(a), when the OCT technique is disabled, the settling time (t_s) for the system is around 1.1s. When the OCT technique is activated during the startup period, which can rapidly approximate the maximum power point, the settling time can be shorten to 22ms, as shown in Fig. 5.33(b). Therefore, the tracking speed is improved with the proposed MPPT algorithm and circuit.

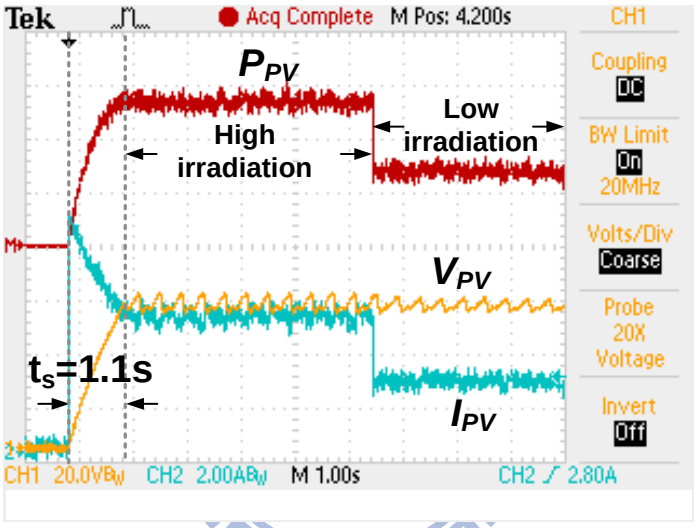

(a)

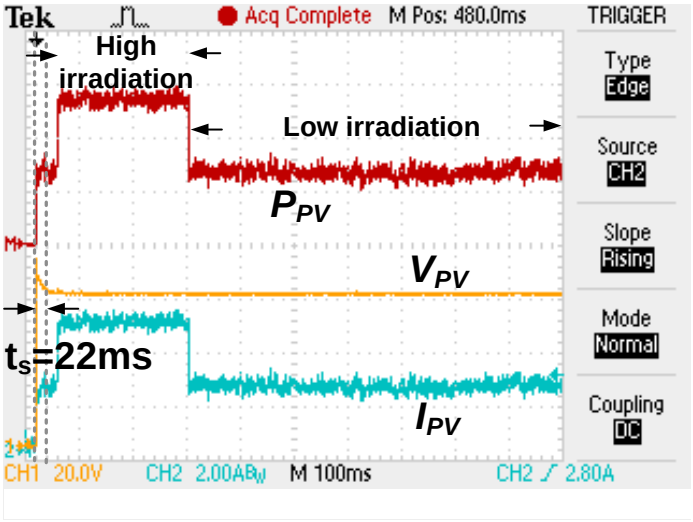

(b)

Fig. 5.33 The waveforms of V_{PV}, I_{PV} and P_{PV} during the power-on period. (a) When the OCT technique is disabled. (b) When the OCT technique is activated.

Fig. 5.34(a) shows the waveforms at the output of DC-AC inverter which is connected to the boost converter. Fig. 5.34(b) demonstrates that when the grid-connected PV system is enabled, the output voltage V_{AC} works in phase with the grid power V_{Grid}. TABLE 5.4 summarizes the measurement results. The proposed AMPPT technique can achieve a tracking efficiency of 97.3%.

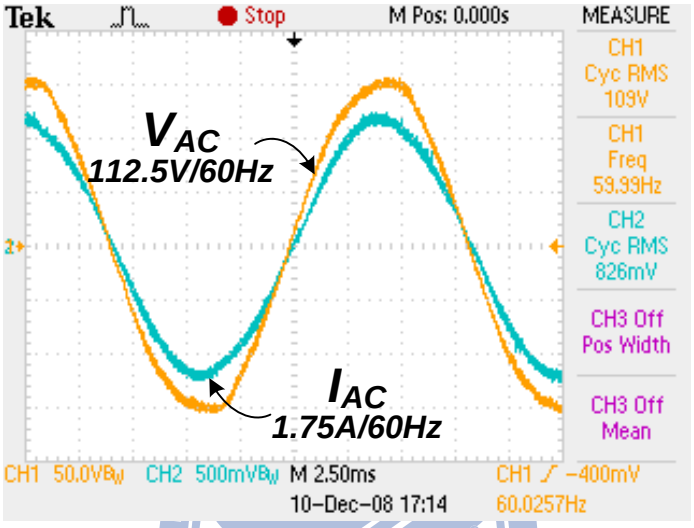

(a)

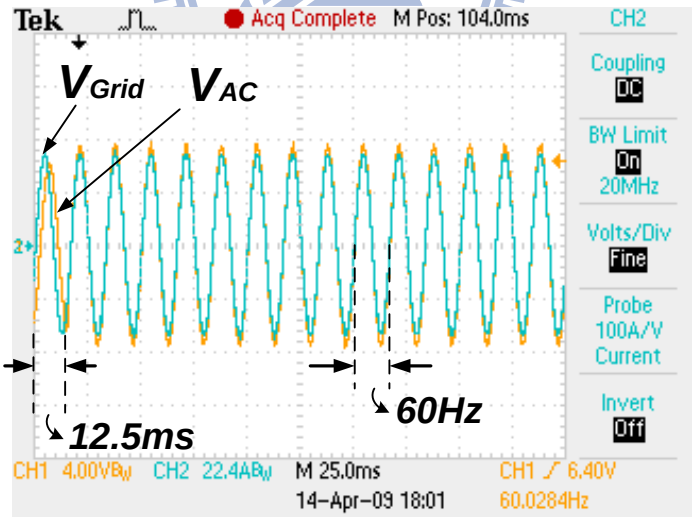

(b)

Fig. 5.34 The waveforms of the DC-AC inverter. (a) Output voltage and current of the inverter. (b) Output waveforms when V_{AC} is connected to V_{Grid}.

TABLE 5.4 Design Specifications

Fabrication Process	0.25μm BCD 40V 1P4M
Chip area	$4.22mm^2$
Inductor	L_1=5mH, L_2=5mH
Capacitor	C_1=1500μF, C_2=50μF
Switching frequency	120kHz
Nominal AC output voltage	112V
Power factor	0.998
Tracking efficiency	>97.3% (@P_{PV}=100W~285W)
Overall efficiency	88.97%
Input Capacitor	C_{pv}=4700μF

Chapter 6

Conclusion and Future Work

Several MPPT algorithms and the characteristics of solar arrays are discussed first in this thesis to help understand the behaviors of solar array, which is useful while designing the maximum power point tracking circuit. The proposed maximum power point tracking algorithm, which basically combine two tracking algorithms, can not only achieve fast tracking speed but also maintain high tracking efficiency in a solar electricity system. Furthermore, with analog circuit implementation, power consumption can be reduced and high power efficiency of the system is ensured as a result. A wide-range current multiplier circuit is implemented to meet the requirement of the tracking circuit. The proposed MPPT circuit can determine the slope condition with fast speed and high accuracy. In the end, simulation and experiment results verify the efficiency and the tracking speed of the proposed MPPT algorithm. The experiment results, moreover, demonstrate that the PV system can also convert solar energy into grid electricity with synchronized phase response.

The tracking speed and tracking efficiency of the proposed tracking technique can be further improved when the variable perturbation steps are included. When the operating point is far away from the maximum power point, the perturbation step can be set as a larger one to increase the tracking speed. While the operating point is near the maximum power point, the perturbation can be switched to a smaller one to ensure the minimum oscillation and therefore a high tracking efficiency.

Reference

[1] H. Chun-Yu and C. Ke-Horng, "Boost DC-DC Converter With Fast Reference Tracking (FRT) and Charge-Recycling (CR) Techniques for High-Efficiency and Low-Cost LED Driver," *Solid-State Circuits, IEEE Journal of*, vol. 44, pp. 2568-2580, 2009.

[2] A. Richelli, *et al.*, "A 0.2V-1.2V DC-DC Boost Converter for Power Harvesting Applications," *Power Electronics, IEEE Transactions on*, vol. 24, pp. 1541-1546, 2009.

[3] E. Carlson, *et al.*, "20mV input boost converter for thermoelectric energy harvesting," in *VLSI Circuits, 2009 Symposium on*, 2009, pp. 162-163.

[4] C. Zhe, *et al.*, "A Review of the State of the Art of Power Electronics for Wind Turbines," *Power Electronics, IEEE Transactions on*, vol. 24, pp. 1859-1875, 2009.

[5] W. Rong-Jong and W. Wen-Hung, "Grid-Connected Photovoltaic Generation System," *Circuits and Systems I: Regular Papers, IEEE Transactions on*, vol. 55, pp. 953-964, 2008.

[6] G. J. Bauhuis, *et al.*, "26.1% thin-film GaAs solar cell using epitaxial lift-off," *Solar Energy Materials and Solar Cells*, vol. 93, pp. 1488-1491, 2009.

[7] M. A. Green, *et al.*, "Solar cell efficiency tables (version 36)," *Progress in Photovoltaics: Research and Applications*, vol. 18, pp. 346-352, 2010.

[8] T. Esram, *et al.*, "Dynamic Maximum Power Point Tracking of Photovoltaic Arrays Using Ripple Correlation Control," *Power Electronics, IEEE Transactions on*, vol. 21, pp. 1282-1291, 2006.

[9] S. Jain and V. Agarwal, "A Single-Stage Grid Connected Inverter Topology for Solar PV Systems With Maximum Power Point Tracking," *Power Electronics, IEEE Transactions on*, vol. 22, pp. 1928-1940, 2007.

[10] F. Boico, *et al.*, "Solar Battery Chargers for NiMH Batteries," *Power Electronics, IEEE Transactions on*, vol. 22, pp. 1600-1609, 2007.

[11] T. Esram and P. L. Chapman, "Comparison of Photovoltaic Array Maximum Power Point Tracking Techniques," *Energy Conversion, IEEE Transactions on*, vol. 22, pp. 439-449, 2007.

[12] C. Rodriguez and G. A. J. Amaratunga, "Analytic Solution to the Photovoltaic Maximum Power Point Problem," *Circuits and Systems I: Regular Papers, IEEE Transactions on*, vol. 54, pp. 2054-2060, 2007.

[13] K. Jung-Min, *et al.*, "Three-Phase Photovoltaic System With Three-Level

Boosting MPPT Control," *Power Electronics, IEEE Transactions on*, vol. 23, pp. 2319-2327, 2008.

[14] N. Khaehintung, *et al.*, "FPGA Implementation of MPPT Using Variable Step-Size P&O Algorithm for PV Applications," in *Communications and Information Technologies, 2006. ISCIT '06. International Symposium on*, 2006, pp. 212-215.

[15] W. Wenkai, *et al.*, "DSP-based multiple peak power tracking for expandable power system," in *Applied Power Electronics Conference and Exposition, 2003. APEC '03. Eighteenth Annual IEEE*, 2003, pp. 525-530 vol.1.

[16] L. Zhigang, *et al.*, "A new cost-effective analog maximum power point tracker for PV systems," in *Energy Conversion Congress and Exposition (ECCE), 2010 IEEE*, 2010, pp. 624-631.

[17] P. Mattavelli, *et al.*, "A simple mixed-signal MPPT circuit for photovoltaic applications," in *Applied Power Electronics Conference and Exposition (APEC), 2010 Twenty-Fifth Annual IEEE*, 2010, pp. 953-960.

[18] K. K. Tse, *et al.*, "A novel maximum power point tracker for PV panels using switching frequency modulation," *Power Electronics, IEEE Transactions on*, vol. 17, pp. 980-989, 2002.

[19] H. S. H. Chung, *et al.*, "A novel maximum power point tracking technique for solar panels using a SEPIC or Cuk converter," *Power Electronics, IEEE Transactions on*, vol. 18, pp. 717-724, 2003.

[20] R. Leyva, *et al.*, "MPPT of photovoltaic systems using extremum - seeking control," *Aerospace and Electronic Systems, IEEE Transactions on*, vol. 42, pp. 249-258, 2006.

[21] P. Joung-Hu, *et al.*, "Dual-Module-Based Maximum Power Point Tracking Control of Photovoltaic Systems," *Industrial Electronics, IEEE Transactions on*, vol. 53, pp. 1036-1047, 2006.

[22] D. Brunelli, *et al.*, "Design of a Solar-Harvesting Circuit for Batteryless Embedded Systems," *Circuits and Systems I: Regular Papers, IEEE Transactions on*, vol. 56, pp. 2519-2528, 2009.

[23] A. Tariq and J. Asghar, "Development of an Analog Maximum Power Point Tracker for Photovoltaic Panel," in *Power Electronics and Drives Systems, 2005. PEDS 2005. International Conference on*, 2005, pp. 251-255.

[24] D. Sera, *et al.*, "Improved MPPT Algorithms for Rapidly Changing Environmental Conditions," in *Power Electronics and Motion Control Conference, 2006. EPE-PEMC 2006. 12th International*, 2006, pp. 1614-1619.

[25] C.-x. Liu and L.-q. Liu, "An improved perturbation and observation MPPT method of photovoltaic generate system," in *Industrial Electronics and*

Applications, 2009. ICIEA 2009. 4th IEEE Conference on, 2009, pp. 2966-2970.

[26] G. J. Yu, *et al.*, "A novel two-mode MPPT control algorithm based on comparative study of existing algorithms," in *Photovoltaic Specialists Conference, 2002. Conference Record of the Twenty-Ninth IEEE*, 2002, pp. 1531-1534.

[27] C. Dorofte, *et al.*, "A combined two-method MPPT control scheme for grid-connected photovoltaic systems," in *Power Electronics and Applications, 2005 European Conference on*, 2005, pp. 10 pp.-P.10.

[28] C. Yaow-Ming, *et al.*, "The AC Line Current Regulation Strategy for the Grid-Connected PV System," *Power Electronics, IEEE Transactions on*, vol. 25, pp. 209-218, 2010.

[29] P. Maffezzoni and D. D'Amore, "Compact Electrothermal Macromodeling of Photovoltaic Modules," *Circuits and Systems II: Express Briefs, IEEE Transactions on*, vol. 56, pp. 162-166, 2009.

[30] M. G. Villalva, *et al.*, "Comprehensive Approach to Modeling and Simulation of Photovoltaic Arrays," *Power Electronics, IEEE Transactions on*, vol. 24, pp. 1198-1208, 2009.

[31] N. Femia, *et al.*, "Optimization of perturb and observe maximum power point tracking method," *Power Electronics, IEEE Transactions on*, vol. 20, pp. 963-973, 2005.

[32] M. A. S. Masoum, *et al.*, "Theoretical and experimental analyses of photovoltaic systems with voltageand current-based maximum power-point tracking," *Energy Conversion, IEEE Transactions on*, vol. 17, pp. 514-522, 2002.

[33] T. Shimizu, *et al.*, "Generation control circuit for photovoltaic modules," *Power Electronics, IEEE Transactions on*, vol. 16, pp. 293-300, 2001.

[34] H. Patel and V. Agarwal, "Maximum Power Point Tracking Scheme for PV Systems Operating Under Partially Shaded Conditions," *Industrial Electronics, IEEE Transactions on*, vol. 55, pp. 1689-1698, 2008.

[35] X. Weidong, *et al.*, "Topology Study of Photovoltaic Interface for Maximum Power Point Tracking," *Industrial Electronics, IEEE Transactions on*, vol. 54, pp. 1696-1704, 2007.

[36] J. C. Wiles and D. L. King, "Blocking diodes and fuses in low-voltage PV systems," in *Photovoltaic Specialists Conference, 1997., Conference Record of the Twenty-Sixth IEEE*, 1997, pp. 1105-1108.

[37] M. A. de Blas, *et al.*, "Selecting a suitable model for characterizing photovoltaic devices," *Renewable Energy*, vol. 25, pp. 371-380, 2002.

[38] Tynsolar, "http://www.tynsolar.com.tw/upload/TYN-285P6.pdf."

[39] H. Patel and V. Agarwal, "MPPT Scheme for a PV-Fed Single-Phase Single-Stage Grid-Connected Inverter Operating in CCM With Only One Current Sensor," *Energy Conversion, IEEE Transactions on*, vol. 24, pp. 256-263, 2009.

[40] RefuSol. (2010) Königsmörder. *Photon Profi, Photovoltaik-Fachwissen für die Praxis*. 51. Available: http://www.photon.info